Investigating Chandra X-ray sources in the Galactic Bulge with Magellan LDSS2 spectra

Xavier Koenig,[1] Jonathan E. Grindlay,[1] Maureen van den Berg,[1] Silas Laycock,[1] Ping Zhao,[1] JaeSub Hong[1] and Eric M. Schlegel[2]

ABSTRACT

We have carried out optical and X-ray spectral analysis on a sample of X-ray detected optical sources found in five Galactic-bulge fields included in our *Chandra* Multi-wavelength Plane Survey. We use a combination of optical spectral fitting and quantile X-ray analysis to obtain the hydrogen column density towards each object, and a three-dimensional dust model of the Galaxy to obtain a distance in each case. We present the discovery of a population of stellar coronal emission sources, the majority of these likely to be active binaries of RS CVn or BY Dra type. We identify one candidate quiescent low-mass X-ray binary; we note that this object may also likely be an RS CVn system. We report the discovery of three new X-ray detected cataclysmic variables (CVs) in the direction of the Galactic Center (at distances $\lesssim$2kpc). This number is consistent with a local CV space density of $\lesssim 10^{-5}$ pc^{-3}, and a scale height $\sim$200pc, with considerable uncertainty.

Subject headings: surveys — stars: activity — stars: late type — Galaxy: stellar content — novae, cataclysmic variables — X-rays: stars

1. Introduction

The goal of the *Chandra* Multi-wavelength Plane Survey (ChaMPlane)[1] is to study the galactic X-ray point-source population, in particular accretion-powered X-ray sources. ChaMPlane (Grindlay et al. 2003, 2005) comprises two phases of study of the Galactic plane

[1]Harvard-Smithsonian Center for Astrophysics, 60 Garden Street, Cambridge, MA 02138; xkoenig@cfa.harvard.edu

[2]Department of Physics and Astronomy, University of Texas at San Antonio, 1 UTSA Circle, San Antonio, TX 78249

[1]http://hea-www.harvard.edu/ChaMPlane

(Galactic latitudes |b| < 12°): firstly an X-ray survey of serendipitous sources from archival deep *Chandra* X-ray Observatory pointings (with exposure times greater than ∼20ks), and secondly an optical survey in $H\alpha$ (narrow band) and Johnson V, R, and I filters, using the Mosaic imager on the CTIO and KPNO 4m telescopes to image $36' \times 36'$ fields centered on the *Chandra* pointings. Optical spectra are then obtained for classification of candidate optical counterparts to X-ray sources. Infrared (IR) observations are used to identify candidate counterparts in heavily obscured fields.

In this paper we analyze a sample of candidate optical counterparts from five ChaMPlane fields towards the Galactic bulge, using low-resolution optical spectra. All of these fields are within 20° of the Galactic Center (GC), and within 3° of the Galactic plane. Using the optical wavelength region necessarily constrains the scope of this project. Stars at the distance of the GC (∼8 kpc) are hidden behind a hydrogen column density $N_H \sim 0.5$–2.0×10^{23} cm^{-2}, and are thus absorbed by $A_V \gtrsim 25$ ($A_R \gtrsim 19$). Given our optical survey limit of $R = 24$ and this level of extinction, optical counterparts at the GC are unobservable, therefore our work is restricted to foreground (d $\lesssim$ 3 kpc) sources. As a consequence we focus our efforts on two main goals: 1) to identify candidate cataclysmic variables (CVs) through their broad $H\alpha$ line emission and 2) to study the properties of the sample of stellar coronal emission sources that we detect. In doing so we highlight anomalous cases as potential active binary or quiescent low-mass X-ray binary (qLMXB) systems.

The X-ray and optical datasets used in this study, and their reduction, are discussed in §2–5. Initial spectroscopic results are presented in § 6 where we also highlight new techniques developed for our analysis—a simple spectral fitting process to obtain the extinction $E(B-V)$ and thus N_H from the optical spectra, a three-dimensional (3D) dust model of the Galaxy (Drimmel & Spergel 2001) to obtain a distance in any direction given $E(B-V)$, and the X-ray Quantile Color-Color Diagram (QCCD) technique (Hong et al. 2004) for spectral analysis of low count X-ray point sources. Candidate CVs, active binary systems and qLMXBs, and analysis of the sample of coronally emitting stars detected in this dataset are presented in §7 and $9.1. §8 and §9.2 discuss the initial constraints our results place on the space density of CVs and how the derived space density compares with current estimates of the local CV space density (∼10^{-5}pc^{-3}, see Grindlay et al. 2005; Patterson 1998; Warner 1995).

2. The X-ray Dataset

Hong et al. (2005) and Hong et al. (2006, in preparation) describe in detail the process of selecting archival *Chandra* observations for use in the ChaMPlane survey, and subsequent data processing. In summary, source lists from detections in a broad (B_X, 0.3–8.0 keV), soft

(S_X, 0.3–2.5 keV) and hard (H_X, 2.5–8.0 keV) energy band, are cross-correlated to form a master sourcelist. Source properties, like flux and energy quantiles (see §7), are derived in energy bands more appropriate to analysis of low count sources. These conventional bands are defined: S_C (0.5–2.0 keV), H_C (2.0–8.0 keV) and B_C (0.5–8.0 keV). In the following analysis, we consider only X-ray sources of level 1 and above—these being sources unaffected by hot pixels, bad columns or bad bias values on the ACIS detector, or readout streaks from bright sources; this also serves to cut sources too close to the chip boundary; see Hong et al. (2005) for a complete description of the different levels assigned to sources in our X-ray catalogue.

X-ray data for this paper comes from three ACIS-I and one ACIS-S *Chandra* pointings. In addition, we have stacked 14 ACIS-I observations centered on SgrA* to create a deep image of the Galactic Center region. This stack includes the observations analyzed by Muno et al. (2003) (with the exception of ObsID 1561) that amount to a total of 590 ksec exposure time, with the addition of ObsIDs 3549, 4683, 4684 and 5360. The resultant total exposure time is 748ks (which results in 698ks of good time interval after processing). The process of dealing with duplicate sources between individual pointings in the stack is detailed in Hong et al. (2005). The final stacked SgrA* observation we label ObsID 53392. It overlaps partially with ObsID 945—the two share 46 X-ray sources in common. All fields listed in Table 1 were observed with *Chandra* ACIS-I except J1655, for which ACIS-S was used. Exposure times given are before correcting for good time intervals (GTI).

Table 1. X-ray Observations used in this Paper

Obs. ID	Field Name	Aimpoint		No. of Sources[a]	Exposure	N_{22}
		$l(^\circ)$	$b(^\circ)$	B_X, H_X, S_X	(ks)	(cm^{-2})[b]
99	GRO J1655−40 (J1655)	344.98178	2.45612	137	43.0	0.7
737	G347.5−0.5b (G347b)	347.36606	−0.85734	108	40.0	1.8
944	SgrB2	0.58834	−0.02491	369	100.0	82.0
945	Gal. Center Arc (GalCA)	0.14055	−0.09707	222	50.0	50.0
53392[c]	SgrA⋆	359.94415	−0.04594	2982	748.0	48.5

[a]Number of valid (level 1) sources found in the B_X band.

[b]Full column density N_H in units of 10^{22} through entire Galaxy, from Schlegel et al. (1998).

[c]ObsID 53392 is a number we assign internally to refer to our stacked SgrA⋆ observation.

3. Spectroscopic Target Selection and Observations

Targets for optical spectral follow-up were selected following observations made in March 2000 with the Mosaic camera on the CTIO 4m telescope in V, R, I and $H\alpha$ filters to identify candidate counterparts (see Zhao et al. 2005, for details). The resultant optical photometric catalogue was combined with our X-ray source lists to make a target list for the observing runs in 2001–2002 with the Low Dispersion Survey Spectrograph 2 (LDSS2) on the 6.5m Baade Magellan telescope; details of the runs are given in Table 2. For the two 2001 epochs, *Chandra* positions were matched against the appropriate Mosaic image without any boresight correction; optical sources within $4''$ of a *Chandra* position were considered a match and were included in the target list. For the 2002 run, a first order estimate of the boresight correction to the X-ray positions was obtained by matching *Chandra* X-ray positions against USNOA2 catalogue sources falling within their 95% confidence error circle, taking an average of the offsets between these, then excluding matches with offsets more than one standard deviation from the mean and finally re-computing the mean offset. This boresight correction was then applied to the X-ray positions in order to create a target list of matches in the optical database from Mosaic observations. A more refined boresight analysis (see Zhao et al. 2005) was applied for the analysis presented in this paper, see §5.

The LDSS2 instrument[2] uses a multi-aperture mask with a $\sim 5'$ diameter field of view. With a dispersion of 5.3Å per pixel, we obtained spectra centered on 6500Å covering ∼3500 to 9500Å at a resolution of 13.3Å. Masks for LDSS2 were generated with the *ldss2mask.f* FORTRAN code. Using slit lengths between ∼5 and $10''$, and 3 or 4 alignment stars, between 6 and ∼20 targets were assigned to each mask. Given the ChaMPlane goal of finding X-ray binaries, largely powered by accretion processes, highest priority for inclusion of targets on the masks went to objects showing both X-ray and $H\alpha$ emission (i.e. $H\alpha - R < -0.3$), followed by X-ray source candidate optical counterparts (regardless of X-ray or optical colors), then $H\alpha$ bright objects ($H\alpha - R < -0.3$), and then 'marginal' $H\alpha$ objects (with $-0.3 < H\alpha - R < -0.2$). Each of these groups was sorted in order of R-magnitude brightness,

[2]http://www.ociw.edu/lco/magellan/instruments/LDSS2/ldss2_usersguide.html

Table 2. Spectral Observations with LDSS2/Magellan 6.5m

Date	Fields Observed	Flux Standards Used	Grism/Filter
May 18–20 2001	SgrA	LTT3864, LTT7987	MedRed/S2
July 25–27 2001	SgrB2	LTT9239, Feige110, LTT7379	MedBlue/None
June 16–19 2002	J1655, GalCA, SgrA, SgrB2, G347b	LTT9239, EG274	MedBlue/None

with brightest objects having highest priority. We observed 334 targets within the *Chandra* fields of view across all five fields, of which we consider 135 to be 2σ matches based on the procedure outlined in §5 (see table 3, below).

4. Reduction

Data from LDSS2 were reduced using the standard IRAF procedure *ccdproc*. Spectra were extracted one-by-one using the IRAF *doslit* package. When crowding in dense fields resulted in multiple stars falling on a slit, the correct target star was identified for extraction by comparing the dispersed CCD image of the spectra with the Mosaic image of the field and a reference image of the sky taken without the LDSS2 slit mask and grism in place. Stars too poorly exposed to find any trace on the CCD, too badly saturated, or on incorrectly cut slits were not extracted (this was the case for ∼20% of the targets). Flux calibration was performed on each extracted spectrum using IRAF routines. Flux standard spectra were taken each night.

Where possible, all extracted spectra were then assigned a spectral classification by visual inspection and comparison with published atlases of optical and near-IR spectra (Torres-Dodgen & Weaver 1993; Jacoby et al. 1984; Carquillat et al. 1997; Andrillat et al. 1995). These classifications are presented in table 4 in § 6 below.

5. Combining the Datasets: X-ray to Optical Matching

We determine the systematic offsets between the Chandra and Mosaic astrometries, i.e. the boresight correction, for each pair of X-ray and optical images using the iterative procedure described in Zhao et al. (2005). After applying the boresight correction, we look for candidate optical counterparts within some confidence radius of each X-ray source, taking into account optical and X-ray astrometric uncertainties and the boresight error. We elected to search within a 2 σ radius of each source (thus losing on average ∼5% of the real counterparts).

Table 3 summarizes the statistics of the matching process for each field. We present identifications of matches observed with LDSS2 in table 4. Note that the optical photometry for the matches of ObsIDs 944, 945 and 53392 comes from data from our 2003 CTIO Mosaic run (see Zhao et al. 2005) in place of data from 2000. For each source in Table 4 we list the X-ray ID and optical ID number (columns [1] and [2]). We then give the source properties: spectral classification (column [3]), net X-ray source counts in the B_X band (column [4]),

the hydrogen column density N_H, as derived from our fitting technique, see §6.1 (column [5]), the unabsorbed X-ray to optical flux ratio in the S_C band, adopting a 1.0 keV MEKAL X-ray spectral model (column [6]. See § 2 for band definitions). The distance (see § 6.2) and the derived absolute visual magnitude M_V are in columns (7) and (8). We then give X-ray luminosity, followed by the optical R magnitude and the number of optical sources found to match this X-ray position (columns [9], [10] and [11]). Column (12) gives the X-ray 2 σ search radius size in arcseconds and column (13) gives the offset of the optical position in arcsec from the center of the X-ray error circle. Column (14) gives the expected number of optical sources that should fall in an error circle of this size by chance, given the observed surface density of stars within 1 arcmin of the X-ray position on the Mosaic image. Almost all X-ray sources in Table 4 have only one candidate optical counterpart. Two objects in the J1655 field, (7_055 and 7_058), one in the G347b field (2_012) and three in the SgrB2 field (0_058, 2_055 and 3_095) are matched with multiple optical sources. The 'Classification' column follows the following scheme: mid G means G4–G6, late G: G6–G8, F/G: F8–G2 and so on. A question mark placed next to a classification indicates that the uncertainty in spectral type is greater so mid G? means G3–G7 and F/G? means F7–G3. A star classified as G? means G0–G9 (and equivalently for other types).

Table 3. X-ray to Optical Matching Summary

Field Name	N(X)[a]	N(Xmatch)[b]	N(Opt)[c]	N(Spectra)[d]	N(Id. Spec.)[e]
J1655	137	58	227	32	28
G347b	108	53	147	26	25
SgrB2	369	112	165	52	44
GalCA	222	48	67	9	9
SgrA⋆	2982	327	340	16	14
Total	3818	598	946	135	120

Note. — [a]The number of unique (level 1) X-ray sources in all bands. [b]The number of X-ray sources that have any optical counterpart(s). [c]The number of optical sources falling inside 2σ error circles. Some X-ray sources match multiple optical sources. [d]The number of optical spectra of *Chandra* matches obtained with LDSS2. [e]The number of *identifiable* spectra from this sample.

Table 4. Combined Results

SrcID[a] (1)	OptID (2)	Type[b] (3)	Counts[c] (4)	N_H (5)	$\log(F_x/F_R))$[d] (6)	Dist.[e] (7)	M_V (8)	$\log(L_x)$[f] (9)	R (10)	NM[g] (11)	Search (12)	Offset (13)	P(Ran) (14)
J1655													
B6_001	411192	midM dMe	12±5	0.23±0.23	−1.5±0.5	1.3	8.74±1.73	29.58±0.7	19.58(1)	1	0.972	0.920	0.087
B6_003	362749	mid/lateG	41±8	0.32±0.20	−2.6±0.5	1.7	3.21±1.54	30.43±0.7	15.75(1)	1	0.668	0.232	0.042
B6_004	358172	early/midG	13±5	0.79±0.19	−2.8±0.5	3.9	···	31.00±1.1	17.45(1)	1	0.601	0.380	0.032
B6_005	436006	?	21±6	<1.0	> −1.9	<6.3	>1.71	<31.7	20.02(1)	1	1.500	0.208	0.324
B6_007	422453	early/midK	10±5	0.04±0.14	−3.2±0.4	0.2	···	27.85±0.8	15.33(1)	1	1.519	0.217	0.317
B6_010	400332	?	11±5	<0.01†	···	<0.1	>15.7	<27.0	···	1	1.673	0.650	0.511
B6_012	368963	?	22±6	<0.5†	> −1.0	<2.5	>7.86	<30.5	21.33(3)	1	1.647	1.257	0.406
B6_014	341983	midG	86±10	0.44±0.11	···	2.2	2.50±0.96	31.00±0.7	···	1	0.724	0.170	0.056
B7_001	319684	lateG	23±6	0.29±0.11	−2.2±0.4	1.6	5.62±0.92	29.90±0.7	17.77(1)	1	0.456	0.197	0.015
B7_002	306209	earlyM dMe?	24±6	0.38±0.11	−0.9±0.4	2.0	···	30.04±0.7	21.50(5)	1	0.444	0.237	0.013
B7_003	302832	F3–6IV	64±9	0.58±0.10	−2.9±0.4	2.8	1.17±0.91	30.86±0.7	16.14(1)	1	0.412	0.218	0.015
B7_009	367291	early/midK	6*±4	0.23±0.10	−2.8±0.4	1.3	6.07±0.89	29.18±0.7	17.25(1)	1	0.814	0.169	0.072
B7_012	356466	midM? dMe	9±4	0.46±0.11	−1.3±0.4	2.3	7.97±0.93	30.03±0.7	21.14(2)	1	0.635	0.105	0.029
B7_015	325692	K/M	9±4	0.16±0.09	−2.2±0.4	0.9	8.11±0.85	28.99±0.7	18.19(2)	1	0.625	0.474	0.036
B7_016	325171	G/K	21±6	0.80±0.19	−2.7±0.5	4.0	1.15±1.49	31.05±1.2	17.64(1)	1	0.636	0.451	0.046
B7_017	318011	midlateG	14±5	0.41±0.37	−2.5±0.8	2.1	4.18±2.76	30.08±0.8	17.58(1)	1	0.484	0.275	0.017
B7_018	316446	midM dMe	17±5	0.18±0.10	−1.2±0.4	1.1	10.63±0.85	29.26±0.7	20.56(1)	1	0.711	0.360	0.055
B7_019	315708	earlyG	8*±4	0.42±0.20	−2.7±0.5	2.2	4.32±1.54	29.88±0.8	17.77(1)	1	0.511	0.268	0.017
B7_025	294537	early/midM	15±5	0.21±0.23	−2.4±0.6	1.2	6.75±1.73	29.46±0.7	17.45(1)	1	0.842	0.211	0.081
B7_026	291860	F/G?	6*±4	0.63±0.10	−2.5±0.5	3.1	4.09±0.91	30.12±0.8	19.20(1)	1	0.584	0.230	0.024
B7_027	289290	midM dMe?	18±5	0.18±0.10	−1.3±0.4	1.1	9.85±0.85	29.43±0.7	19.93(2)	1	0.677	0.380	0.050
B7_028	275985	G?	11±5	0.88±0.19	−3.5±0.7	4.5	0.76±1.49	30.38±5.9	17.96(1)	1	0.874	0.322	0.092
B7_029	263293	F/G?	18±6	0.70±0.24	−1.8±0.6	4.0	4.70±1.82	30.59±0.8	20.63(1)	1	0.715	0.692	0.064
B7_036	368658	mid/lateF	7*±4	0.22±0.10	−3.4±0.4	1.3	···	29.15±0.7	15.92(1)	1	1.152	0.210	0.183
B7_042	301269	early/midM dMe	9±4	0.26±0.26	−1.8±0.6	1.4	···	29.40±0.8	19.58(2)	1	0.698	0.399	0.052
B7_043	293753	midM	6*±4	0.13±0.09	−2.1±0.5	0.8	10.04±0.82	28.50±0.8	19.25(1)	1	1.045	0.510	0.163
B7_044	287398	earlyG	8*±5	0.92±0.19	−2.8±0.6	4.8	1.64±1.50	30.81±5.4	19.10(3)	1	1.322	0.358	0.271
B7_046	283242	lateF	9*±5	0.37±0.20	−3.1±0.5	1.9	···	29.87±0.7	16.30(1)	1	0.933	0.391	0.113
B7_047	258057	earlyK	8±5	0.27±0.10	−2.2±0.4	1.5	6.77±0.85	29.46±0.7	18.44(1)	1	0.858	0.788	0.082
B7_050	221609	G/K	11±5	0.26±0.10	−2.5±0.4	1.4	5.67±0.85	29.54±0.7	17.48(1)	1	1.199	0.420	0.207
B7_055	338206	?	13±6	<3.5	> −1.3	<2.4	>7.43	<30.2	20.87(1)	3	2.172	1.383	0.950
B7_058	256020	midM dMe?	12±5	0.24±0.20	−1.8±0.5	1.4	8.34±1.54	29.43±0.8	19.32(1)	2	1.886	1.271	0.712
G347b													
B1_001	167282	lateG	22±6	0.62±0.10	−2.4±0.4	2.3	3.83±0.91	30.53±0.6	17.92(2)	1	0.961	0.173	0.104
B1_002	154326	G?	9*±5	1.32±0.15	−2.7±0.6	4.2	1.76±1.25	30.98±0.7	20.22(1)	1	2.043	1.002	0.456
B1_008	148477	lateG	25±8	0.64±0.10	−2.6±0.5	2.4	4.03±0.91	30.32±0.7	18.22(2)	1	2.190	0.790	0.514
B2_001	297926	midG	9±5	0.63±0.10	−2.2±0.5	2.7	4.72±0.91	30.33±0.6	19.23(1)	1	0.768	0.437	0.063
B2_004	334126	early/midG	14±5	0.56±0.10	−2.1±0.4	2.5	4.88±0.90	30.44±0.6	18.75(1)	1	0.934	0.418	0.063
B2_007	315827	M5	19±7	0.20±0.23	−2.1±0.5	1.1	7.33±1.73	29.71±0.6	17.32(1)	1	1.100	0.770	0.114
B2_012	282357	F/G	5*±4	0.51±0.11	−3.1±0.5	2.2	3.21±0.97	30.05±0.6	16.86(1)	2	0.793	0.354	0.077
B2_013	281218	lateG	17±5	0.68±0.19	−2.8±0.5	2.8	1.42±1.48	30.98±0.6	16.45(1)	1	0.644	0.364	0.048
B2_014	268928	lateK	13±5	0.70±0.21	−2.6±0.5	2.9	3.02±1.59	30.82±0.6	17.59(3)	1	0.577	0.556	0.040
B2_015	267161	G?	56±9	0.60±0.18	···	2.5	5.89±1.44	31.04±0.5	20.05(3)	1	0.691	0.343	0.054
B2_017	259970	K/M dMe	12±5	0.49±0.11	−1.4±0.4	2.2	7.52±0.97	30.19±0.6	20.46(1)	1	1.386	1.020	0.224
B2_019	252101	midG	8*±4	0.74±0.21	−3.1±0.6	3.0	1.79±1.60	30.58±0.6	16.954(4)	1	0.571	0.474	0.026
B2_020	243055	mid/lateG	20±6	0.47±0.20	−2.1±0.5	2.1	···	30.55±0.6	17.72(2)	1	0.653	0.371	0.048
B2_023	265728	G/K?	12*±6	0.75±0.19	−2.5±0.5	3.0	2.61±1.49	30.81±0.6	17.993(4)	1	1.630	1.219	0.271
B2_028	303928	lateA	14±6	0.42±0.20	−3.1±0.5	1.8	3.12±1.54	30.00±0.6	15.98(1)	1	2.004	1.086	0.404

Table 4—Continued

SrcID[a] (1)	OptID (2)	Type[b] (3)	Counts[c] (4)	N_H (5)	$\log(F_x/F_R))$[d] (6)	Dist.[e] (7)	M_V (8)	$\log(L_x)$[f] (9)	R (10)	NM[g] (11)	Search (12)	Offset (13)	P(Ran) (14)
B3_007	311764	midG	18±6	0.72±0.11	−1.1±0.4	3.0	6.45±0.95	30.94±0.6	21.15(3)	1	1.343	0.678	0.189
B3_011	289209	lateG?	18±6	1.03±0.63	−3.0±1.2	3.6	1.01±4.65	31.03±0.7	17.94(2)	1	0.609	0.535	0.042
B3_013	255901	F/G?	9±4	0.75±0.11	−2.3±0.6	3.0	4.19±0.95	30.36±0.7	19.73(1)	1	0.692	0.337	0.059
B3_014	243850	earlyG	10±5	0.61±0.10	−2.6±0.5	2.7	3.97±0.91	30.22±0.6	18.33(1)	1	0.517	0.299	0.027
B3_016	242465	TTauri	12±5	0.64±0.10	−2.5±0.4	2.7	3.35±0.91	30.61±0.6	17.94(2)	1	0.760	0.425	0.068
B3_020	328280	earlyG	11±5	0.47±0.11	−2.7±0.4	2.1	3.58±0.93	30.25±0.6	16.94(2)	1	1.079	0.288	0.099
B3_024	231576	earlyA	13±5	0.48±0.24	−3.4±0.6	2.1	···	30.34±0.6	14.96(1)	1	0.655	0.639	0.049
B3_025	229112	lateF?	8*±4	0.85±0.11	−2.2±0.5	3.4	3.70±0.96	30.63±0.6	19.87(1)	1	1.128	0.555	0.158
B3_026	223728	earlyK	10±5	1.07±0.12	···	3.7	3.74±1.09	30.94±0.6	21.02(5)	1	0.756	0.256	0.069
B3_027	221231	?	8*±4	>10.0	···	···	···	···	21.84(4)	1	1.170	0.650	0.168
B3_028	205013	lateF	11±5	0.55±0.10	−2.2±0.5	2.0	5.65±0.90	29.96±0.7	19.28(2)	1	1.011	0.475	0.116
SgrB2													
B0_002	42992	lateG	120±14	0.63±0.19	−2.7±0.5	1.0	3.73±1.48	30.25±1.5	15.93(1)	1	1.091	0.587	0.104
B0_005	28687	?	62±9	2.32±0.23	···	2.5	−34.96±32.4	···	20.42(2)	1	0.533	0.393	0.023
B0_007	27479	lateF	12±5	0.20±0.20	−4.1±0.5	0.4	5.95±1.54	28.05±1.9	14.21(1)	1	0.821	0.141	0.052
B0_011	18587	K/M dMe	31±8	0.36±0.20	−2.1±0.5	0.6	8.39±1.54	29.11±1.6	18.13(1)	1	0.977	0.101	0.075
B0_012	18430	midK	19±6	0.14±0.16	−2.2±0.4	0.3	11.06±1.27	28.01±2.1	17.91(1)	1	0.504	0.250	0.012
B0_015	303055	G/K	53±9	0.82±0.19	−2.2±0.5	1.2	4.84±1.49	30.26±1.3	18.45(1)	1	0.812	0.115	0.026
B0_017	288069	F/G?	8*±4	1.00±0.12	−3.1±0.6	1.4	5.10±1.08	29.26±1.4	19.86(1)	1	0.575	0.219	0.023
B0_020	45181	midK	20±8	0.17±0.19	−2.3±0.5	0.3	10.15±1.50	28.28±2.0	17.49(2)	1	1.699	0.575	0.183
B0_023	40690	lateF?	48±11	0.44±0.11	−4.0±0.4	0.8	1.73±0.96	29.65±1.5	12.98(1)	1	1.994	1.531	0.123
B0_025	38933	TTauri	53±10	0.46±0.20	−2.7±0.5	0.8	5.37±1.51	29.71±1.5	16.14(1)	1	1.559	0.884	0.149
B0_035	25063	?	10±5	2.38±0.23	−7.0±6.1	2.5	···	31.60±1.8	20.09(2)	1	0.941	0.437	0.077
B0_045	37793	mid/lateF	18±7	0.52±0.19	−2.9±0.5	0.9	6.94±1.47	28.93±1.5	18.15(1)	1	3.011	0.390	1.673
B0_048	26302	?	24±8	>10.0†	···	>6.0	···	···	20.77(2)	1	2.477	1.219	0.388
B0_052	55364	earlyG	20*±10	0.80±0.11	···	1.2	5.03±0.96	···	18.44(1)	1	2.483	1.400	0.826
B0_053	45577	?	43±11	<2.0†	>2.5	<2.3	>0.86	<31.0	21.61(2)	1	1.689	1.170	0.174
B0_058	24481	lateG?	4*±5	0.88±0.19	···	1.3	6.23±1.49	···	20.07(1)	3	4.128	3.930	1.874
B1_003	19124	?	34±7	0.88±0.24	−7.2±2.8	1.3	−12.22±12.2	30.87±1.3	17.77(2)	1	0.485	0.115	0.016
B1_005	294663	G?	23±6	0.92±0.19	−2.5±0.5	1.3	4.64±1.50	30.00±1.3	18.94(1)	1	0.538	0.287	0.022
B1_007	284945	early/midG	29±7	0.46±0.20	−2.6±0.5	0.8	6.17±1.51	29.39±1.5	17.18(1)	1	0.483	0.197	0.026
B1_008	43818	F/G	116±14	0.25±0.10	−2.4±0.3	0.4	6.86±0.89	29.37±1.7	15.55(1)	1	1.015	0.799	0.050
B1_010	33389	early/midG	34±7	0.48±0.17	−2.7±0.4	0.8	5.80±1.36	29.46±1.5	17.04(1)	1	0.680	0.253	0.025
B1_013	25156	midM dMe	11±5	0.13±0.09	−1.3±0.4	0.3	15.02±0.82	27.70±2.1	20.99(2)	1	0.867	0.207	0.068
B1_016	23005	earlyG	16±6	0.43±0.11	···	0.7	9.52±0.96	···	19.82(2)	1	0.622	0.611	0.023
B1_017	22695	midM dMe	13±5	0.46±0.26	−1.8±0.6	0.8	10.08±1.93	28.97±1.6	20.13(2)	1	0.666	0.233	0.026
B1_019	20349	G/K	11±5	0.64±0.10	−2.7±0.4	1.0	6.13±0.91	29.27±1.5	18.50(1)	1	0.570	0.316	0.036
B1_028	300953	K/M	7±4	0.41±0.11	−2.1±0.4	0.7	9.26±0.96	28.81±1.6	19.45(1)	1	0.733	0.132	0.035
B1_039	41847	K/M dMe	95±12	0.26±0.10	−2.2±0.3	0.5	7.65±0.85	29.35±1.7	16.27(1)	1	1.045	0.409	0.032
B1_047	31055	lateA	7*±5	0.63±0.16	−3.7±0.5	1.1	3.50±1.29	29.16±1.4	16.32(1)	1	1.436	0.318	0.238
B1_048	28460	?	12±5	<3.0†	> −5.1	<3.0	···	<30.0	22.78(6)	1	1.662	0.841	0.937
B1_057	19971	earlyM dMe	18±7	0.36±0.26	−2.2±0.6	0.6	9.20±1.97	28.89±1.6	18.49(1)	1	1.137	0.583	0.185
B1_073	32534	midG	27±9	0.16±0.09	−2.8±0.4	0.3	9.99±0.85	27.87±2.0	17.29(2)	1	2.506	1.621	0.464
B2_011	263355	earlyM dMe?	14±5	0.54±0.24	−1.8±0.6	0.9	9.00±1.86	29.30±1.5	20.05(1)	1	0.906	0.237	0.062
B2_012	261885	F/G?	27±7	0.78±0.19	−2.2±0.5	1.2	6.08±1.49	29.84±1.4	19.35(1)	1	0.972	0.295	0.068
B2_015	250682	F/G?	33±7	0.58±0.18	−2.8±0.5	0.9	4.81±1.44	29.69±1.5	16.709(4)	1	0.647	0.550	0.031
B2_017	280822	F/G	10±5	0.79±0.14	−2.9±0.5	1.2	4.52±1.16	29.68±1.4	18.13(1)	1	0.905	0.199	0.088
B2_033	242458	mid/lateG	12*±6	0.58±0.18	−4.1±1.9	0.9	5.54±1.44	28.10±2.4	17.506(2)	1	1.108	0.696	0.087
B2_037	232688	F/G	25±7	0.39±0.23	−3.7±0.5	0.7	4.05±1.74	29.24±1.6	14.29(1)	1	1.213	1.153	0.100
B2_044	246059	midM dMe	13±6	0.28±0.27	−2.1±0.6	0.5	10.26±2.04	28.53±1.7	18.82(1)	1	2.399	0.899	0.917

Table 4—Continued

SrcID[a] (1)	OptID (2)	Type[b] (3)	Counts[c] (4)	N_H (5)	$\log(F_x/F_R))$[d] (6)	Dist.[e] (7)	M_V (8)	$\log(L_x)$[f] (9)	R (10)	NM[g] (11)	Search (12)	Offset (13)	P(Ran) (14)
B2_055	221198	mid/lateF	25±9	0.84±0.19	−3.3±0.5	1.3	2.59±1.49	30.07±1.3	16.49(2)	2	2.017	1.464	0.282
B3_004	251487	lateG	209±16	0.64±0.21	−3.2±0.5	1.0	1.31±1.63	30.64±1.4	13.99(2)	1	0.458	0.201	0.014
B3_006	239844	F/G	225±16	0.54±0.19	−3.3±0.5	0.9	1.45±1.47	30.47±1.5	13.36(1)	1	0.561	0.419	0.018
B3_008	277618	G?	7⋆±4	0.81±0.19	−2.5±0.5	1.2	5.94±1.49	29.42±1.4	19.78(1)	1	0.564	0.423	0.017
B3_020	263848	midM dMe	444±22	0.19±0.17	−1.4±0.4	0.3	9.70±1.35	29.61±1.9	16.86(2)	1	0.518	0.390	0.020
B3_028	260114	lateG?	13±5	0.55±0.21	−4.4±0.5	0.9	2.40±1.63	29.25±1.5	13.64(8)	1	0.582	0.389	0.017
B3_031	256812	earlyK	17±6	0.62±0.24	−2.5±0.6	1.0	6.82±1.82	29.34±1.5	18.750(4)	1	0.628	0.233	0.026
B3_039	249150	midM dMe	40±8	0.12±0.22	−1.9±0.5	0.2	12.00±1.65	28.17±2.2	17.92(1)	1	0.787	0.410	0.051
B3_040	247543	lateF	32±7	0.62±0.19	−3.3±0.5	1.0	2.71±1.48	29.74±1.5	15.75(9)	1	0.687	0.110	0.033
B3_065	245213	G/K	11±5	0.67±0.27	−2.7±0.6	1.0	6.13±2.02	29.37±1.5	18.52(1)	1	1.015	0.749	0.063
B3_071	234977	K	21±7	2.51±0.43	−5.2±0.9	2.6	−4.00±3.27	30.88±1.2	18.08(1)	1	1.171	0.885	0.072
B3_075	230542	G/K	24±7	0.62±0.21	−2.7±0.5	1.0	5.30±1.63	29.64±1.5	17.57(3)	1	1.146	0.097	0.086
B3_081	274503	midM	17⋆±8	0.14±0.14	−2.7±0.4	0.3	10.48±1.13	27.94±2.1	17.04(3)	1	2.231	1.546	0.438
B3_095	223079	?	33±8	>2.0	< −3.2	>2.3	< −0.09	>30.7	21.18(1)	3	3.641	3.440	1.749
GalCA													
B1_001	147093	lateG	127±13	0.68±0.10	−2.0±0.3	1.1	4.37±0.88	30.70±1.4	16.95(3)	1	0.407	0.258	0.010
B1_005	141411	G?	10⋆±5	0.50±0.19	−2.2±0.5	0.8	7.24±1.51	29.40±1.5	18.45(1)	1	1.161	0.707	0.081
B2_002	196642	CV	438±22	1.4±0.3	−1.2±0.6	1.8	2.78±2.29	31.87±1.2	20.23(2)	1	0.447	0.317	0.013
B2_003	181009	midM	23±6	0.15±0.09	−1.6±0.4	0.3	12.22±0.85	28.41±2.0	18.82(1)	1	0.636	0.096	0.026
B2_016	174087	early/midA	3⋆±4	0.31±0.15	−3.8±0.5	1.1	3.95±1.17	29.09±0.9	15.01(1)	1	0.685	0.027	0.032
B3_003	156844	late/midF	12±5	0.08±0.12	−3.6±0.4	0.2	8.16±1.02	27.62±2.3	14.06(1)	1	0.489	0.137	0.015
B3_007	179593	G?	12±5	0.49±0.19	−1.6±0.5	0.8	8.53±1.51	29.54±1.5	19.56(1)	1	0.594	0.097	0.024
B3_032	195436	midM dMe	13±5	0.00±0.01	−1.6±0.3	0.1	16.58±0.51	26.71±0.2	18.60(1)	1	0.895	0.416	0.057
H2_035	234913	CV	30±12	>1.4	< −2.3	>1.7	<3.99	>30.2	21.30(2)	1	2.36	2.03	0.401
SgrA													
B3_0001	134464	CV	3539±63	0.70±0.40	−0.1±0.9	1.9	7.90±2.96	31.25±0.9	21.77(3)	1	0.430	0.007	0.013
B3_0011	106515	lateG?	831±33	0.32±0.20	−2.3±0.5	1.4	4.40±1.54	30.39±0.7	16.18(2)	1	0.431	0.096	0.015
B3_0035	99283	lateG?	273±22	0.36±0.23	−2.0±0.5	1.4	5.85±1.73	30.21±0.7	17.58(6)	1	0.516	0.014	0.019
B3_0206	83302	midM dMe	202±18	0.12±0.25	−1.5±0.5	0.9	10.51±1.85	29.17±0.5	19.40(1)	1	0.476	0.289	0.012
B3_0219	82858	A/F?	290±22	3.00±1.00	−5.2±1.7	4.5	−6.97±7.36	32.08±0.8	18.45(1)	1	0.383	0.105	0.009
B3_0417	55522	midM dMe	1071±35	0.31±0.26	−1.3±0.6	1.4	7.39±1.93	30.47±0.7	18.22(1)	1	0.429	0.209	0.011
B3_0420	49010	?	728±32	5.80±1.20	−7.6±2.1	11.5	···	33.64±0.7	22.31(5)	1	0.497	0.221	0.015
B3_0823	87298	midM dMe?	36±10	0.55±0.35	−2.2±0.7	1.6	7.45±2.64	29.40±0.9	20.03(1)	1	0.518	0.195	0.017
B3_1466	58767	?	107±14	<0.001†	> −2.3	<0.1	>13.7	<26.9	17.83(1)	1	0.505	0.151	0.013
B3_1525	51314	lateG?	212±19	0.24±0.26	−2.4±0.6	1.3	6.09±1.93	29.75±0.6	17.04(1)	1	0.525	0.111	0.016
H3_0477	118522	G/K	501±34	1.45±0.15	−3.5±0.6	3.2	···	30.04±0.9	20.55(4)	1	0.575	0.506	0.017
S3_014	94670	midM dMe	70±14	0.16±0.25	−2.1±0.5	1.1	9.02±1.92	29.12±0.6	18.62(1)	1	0.519	0.114	0.016
S3_046	66862	midM dMe	136±16	0.00±0.06	−2.0±0.3	0.1	15.78±0.67	26.52±0.0	17.97(1)	1	0.475	0.034	0.011
S3_066	116046	early/midK	185±22	0.39±0.11	−2.3±0.4	1.5	5.96±0.96	29.85±0.7	17.79(1)	1	0.536	0.114	0.019
S3_154	71237	F/G	127±16	0.37±0.26	−2.7±0.6	1.4	5.42±1.97	29.69±0.7	17.17(1)	1	0.556	0.234	0.019
S3_303	42300	K/M dMe	83±18	0.80±0.50	−2.5±0.9	2.3	4.74±3.68	30.21±0.7	19.23(1)	1	0.899	0.868	0.045
B0_041	100283	F/G	89±13	0.31±0.26	···	1.4	5.79±1.32	···	17.28(1)	1	0.980	0.598	0.059

[a]The full *Chandra* SrcID has prefix XS00099, XS00737, XS00944, XS00945, XS53392 respectively. See Table 1 for exposure times.

[b]See table 3 for explanation of spectral type classification.

[c]Background subtracted net counts in the Bx band (0.3–8.0keV). ⋆This source has SNR<3.

[d]log of the ratio of unabsorbed flux in S_C band 0.5–2.0keV to unreddened optical R band flux (ergs cm^{-2} s^{-1} (1000Å)$^{-1}$)

[e]The distance in kpc. Error ≈60%.

[f]log of X-ray luminosity in S_C band (ergs s^{-1})

[g]NM—number of optical matches found within 95% confidence (2σ) error circle.

6. Results

6.1. Modelling the Spectra

We use a 'new' technique in an attempt to derive N_H for all X-ray-optical matches observed with LDSS2. We fit the flux-calibrated *optical* spectrum of each optical counterpart with a blackbody spectrum affected by insterstellar reddening, at an effective temperature (T_{eff}) appropriate to its estimated spectral type derived from our spectra. This fit is independent of any X-ray emission properties. We simulate the effect of interstellar reddening due to dust assuming an average Galactic extinction law $E(\lambda - V)/E(B - V)$ using the analytical parameterization given by Howarth (1983). When assigning temperatures we create rough 'spectral types' to simplify the process. Each bin of spectral types covers roughly 3 to 5 sub-types by temperature. Effective temperatures and adopted photometry for each bin are given in Table 5 below, taken from the references listed in the table. Temperatures were assigned to each bin to be roughly representative of the spectral type range given, while also attempting to account for the fact that luminosity class is uncertain too (i.e. A/F means A8 to F2, luminosity class undetermined). Absolute magnitudes are given for stars on the Main Sequence with an estimate of the expected range for the spectral type bin given.

To convert the model blackbody emission spectrum from a surface flux to an observed flux at the detector, the spectrum is also scaled by a factor R^2/d^2 (radius of object R, distance d). The fitting process thus returns $E(B - V)$ and R^2/d^2, as we keep T_{eff} fixed. To obtain A_V we adopt $A_V = 3.1 \times E(B - V)$. We utilize the observed relation $N_H = 1.79 \times 10^{21} \times A_V$ cm^{-2} of Predehl & Schmitt (1995): to convert this to a hydrogen column density. We limit the region to be fitted to the central part of the spectra: 5500–6700Å; this is in part to simplify the fitting procedure, and also due to the fact that the flux calibrated spectra anomalously fall off in flux redward of ∼7000Å. See § 6.4 below for more discussion of this problem. We also remove (by interpolating over) major spectral lines at 5575, 6300 and 6562Å and, in the case of the molecular bands present in M type stars we fit a smooth continuum shape to the star at 3–4 points between bands (we use a Legendre polynomial of order 10) and fit to this instead. Example fits for a K and an M (polynomial fit) star are shown in Figure 1.

For stars with low signal-to-noise ratio spectra we assign a non-classification to the object '?' in Table 4. In order to place constraints on N_H for these sources, and for the CVs, whose optical spectra are not well modelled by single-temperature blackbodies, we utilize the QCCD technique as discussed in § 7.1. Objects for which this has been carried out are marked with a † in table 4.

Table 5. Effective Temperature Assignment and Photometric Values Used

Classification	Sp. Type Range	T_{eff} (K)	V−R	R−I	M_V
Early A	A2–A4	9100	0.08	0.03	1.8±0.4
Mid A	A4–A6	8500	0.16	0.06	2.0±0.5
Late A	A6–A8	7700	0.19	0.09	2.4±0.6
A/F	A8–F2	7200	0.30	0.17	2.8±0.6
Early F	F2–F4	6750	0.35	0.20	3.2±0.4
Mid F	F4–F6	6500	0.40	0.24	3.5±0.4
Late F	F6–F8	6200	0.47	0.29	3.8±0.4
F/G	F8–G2	5950	0.50	0.31	4.3±0.7
Early G	G2–G4	5600	0.53	0.33	4.6±0.4
Mid G	G4–G6	5400	0.60	0.42	4.9±0.5
Late G	G6–G8	5200	0.64	0.43	5.3±0.5
G/K	G8–K2	5050	0.70	0.48	5.8±1.0
Early K	K2–K4	4700	0.80	0.53	6.7±0.6
Mid K	K4–K6	4300	1.10	0.75	7.4±0.6
Late K	K6–K8	4000	1.15	0.78	8.4±0.6
K/M	K8–M2	3700	1.25	0.93	9.3±1.0
Early M	M2–M4	3400	1.42	1.15	11.1±1.6
Mid M	M4–M6	3000	1.8	1.67	13.2±2.0

Note. — References for colors, temperatures and absolute magnitudes: Johnson (1966), Bessell (1991), Mikami & Heck (1982), Houk et al. (1997), Gray (1992), Cox (2000). We estimate an uncertainty in the assigned T_{eff} values of ±500K, based on the spread of values found in the various references.

6.2. Extinction Model for the Galaxy

After fitting the optical spectra to derive the extinction values, we utilize the 3D extinction model of the Galaxy presented in Drimmel & Spergel (2001) (hereafter D01) to derive distances to the candidate counterparts. D01 describe a three component model for the dust distribution in the Galaxy which is used (via a FORTRAN code, Drimmel et al. 2003, hereafter: D03) to derive the extinction, A_V as a function of distance from the Sun over the whole sky. To account in some way for small scale variations and clumping in the dust density that are smoothed over by the model, the code gives the option of rescaling the derived extinction in each direction by a factor dependent on the residuals between the actual COBE observed flux at 240μm and the model prediction for the same. Final values are based on the re-scaled values for A_V. The spatial resolution on which those re-scaled values can be measured is $\sim$20arcmin. For each of our *Chandra* fields we use the code to derive the run of A_V with distance, see Figure 2. It should be noted that the curves for fields SgrB2 and GalCA are almost identical and hence indistinguishable on this figure. This is almost certainly an artifact of the dust model and not a real trait of these two fields which are $\sim$0.5° apart of the sky, particularly since the curve for field SgrA$\star$ (which is only $\sim$12′ away) is significantly different.

Following the advice of Drimmel et al. (2003) we urge caution in adopting any results for d derived from this model for Galactic longitude $|l|< 20°$. The other output of our spectral fitting procedure, the scaling factor R^2/d^2, is also useful as a sanity check on the process, as we can thus derive a radius for each object, to compare with expected values for stars of given spectral type and M_V (e.g. Cox 2000). It was found that for all fields, using the rescaling option in the D03 code worked well in producing reasonable stellar radii within 50% of tabulated values (e.g. Cox 2000), with the exception of G347b, where radii were systematically a factor of four to five times higher. As a consequence, we replace the above procedure by using our own calculation of $A_V(d)$ for this field. We used CO emission data—kindly provided by Tom Dame, to derive the column density of molecular hydrogen and 21cm HI data to calculate that of atomic hydrogen, and thus N_H via $N_H = N_{HI} + N_{H_2}$. We extracted emission spectra of Galactic molecular CO (from the survey of Dame et al. 2001) and HI diffuse gas (data taken from the Southern Galactic Plane Survey Taylor et al. 2003) to derive A_V along two lines of sight—in Galactic coordinates these are at (l, b): 347.375, -0.75 and 347.375, -0.875 (positions 1 and 2 respectively). The HI data has a resolution of $\sim$1′, but for this analysis was smoothed to 3′ resolution with 2.7′ spacing. Emission from CO was assigned a distance based on line of sight velocity, splitting the near/far ambiguity based on the latitude of observation, and using the Galactic rotation curve of Brand & Blitz (1993). We assumed a FWHM layer thickness for HI of 220pc, and for CO: 120pc. Emission beyond the terminal velocity cutoff was redistributed in a Gaussian below the cutoff with

the Gaussian dispersion equal to the cloud-cloud velocity dispersion: $\sigma(\mathrm{CO}) = 4$ km s^{-1}, $\sigma(\mathrm{HI}) = 8$ km s^{-1}. We assume an atomic hydrogen spin temperature of 140K.

The A_V versus distance plots derived via this method for field G347b are shown on Figure 2, right-hand panel, labelled position 1 and position 2. The large discrepancy between the two plots from the D01 model and the calculation using CO and HI measurements further demonstrates the difficulty in deriving this relation. We were unable to perform the same derivation for the other fields as the three Galactic Center fields (SgrA$\star$, SgrB2 and GalCA) are too close to the Galactic plane to easily assign distances to molecular emission, and for field J1655 the HI data available was not at high enough resolution to accurately run the calculation.

As a further check on the calculation of N_H from spectral fitting, we also perform a simple calculation using our V, R and I photometry. Since for most stars we have V, R and I magnitudes, we can look up the appropriate value for the intrinsic $(V-R)_0$ and $(R-I)_0$ (from Cox 2000) given an adopted spectral type (see Table 5) and calculate $E(V-R) \equiv V - R - (V-R)_0$ and $E(R-I) \equiv R - I - (R-I)_0$. Dopita & Sutherland (2003) give simple relations for the wavelength dependence of interstellar extinction so given some simple algebra we have that: $A_V = 3.97 \times E(V-R)$ and $A_V = 3.76 \times E(R-I)$. We convert to N_H as before in § 6.1. Figure 3 below shows comparisons of the two color-determined values of N_H against this same parameter as derived from the spectral fit method. Although there appears to be a linear correlation between all three estimates of N_H, it can be seen from the plot that the fitting method systematically overestimates the column density relative to either the $V-R$ or $R-I$ derivations by $\sim 3 \times 10^{21}$ cm^{-2}, or $A_V \sim 1.7$. In Figure 4 we construct a color-magnitude diagram for our stellar sources. The absolute visual magnitude M_V and color $V-R$ are dereddened using A_V from the spectral fitting procedure. The main sequence is plotted using the data from Table 5. What this plot shows us is that the stars are being made to look too blue, and from our absolute magnitude values, we find that they are too luminous in addition. A combination of all the sources of error is apparent here. It is likely that we are indeed overestimating A_V from our fitting technique so stars should be fainter and redder. However, incorporating the resultant reduction in distance produced by an A_V of 1.7 would overcompensate in correcting the absolute magnitudes. It is clearly difficult to separate the combined contributions to this error of the spectral-fit-derived A_V and the dust model which is obviously playing a significant role. For the purposes of all subsequent results derived in this paper we bear this in mind, however, but retain our present choices of A_V determination and distance derivation. Note also that a reduction in A_V of 1.7 carried through results in $\Delta \log(F_x/F_V) = +0.3$–$+0.5$ and $\Delta \log(L_x) \sim -0.3$. The exact correction depends on the object's initial N_H.

6.3. Calculating X-ray Fluxes

Absorbed (observed) and unabsorbed X-ray fluxes are derived from net count rates using *sherpa*[3]. For simplicity, we assume that the X-ray radiation produced by the majority of objects in our sample will be emission from a hot (T>10^6 K, kT>0.1 keV) coronal plasma. To calculate fluxes in the hard (H_C) and soft (S_C) bands for each star in our sample we thus adopt a simple single-temperature MEKAL model[4] (bremsstrahlung emission of an optically thin, thermal plasma with metal absorption and emission lines see Mewe et al. 1985) at 1keV and use the N_H value listed in table 4. § 6.4 below discusses the uncertainty introduced by our choice of spectral model on our results for X-ray flux. We derive the X-ray luminosity via $L_x = 4\pi\ d^2\ f_x$ ergs s^{-1}. We list $\log(L_x)$(S_C band) for all sources in table 4. The X-ray to optical flux ratio is calculated via:

$$\log(F_x/F_R) = \log(F_x) + 0.4R + 5.765 \tag{1}$$

and

$$\log(F_x/F_V) = \log(F_x) + 0.4V + 5.426 \tag{2}$$

where we have assumed a square optical filter transmission function of width 1000Å, centered on the quoted filter central wavelength, with an underlying A0 stellar spectrum to calculate the constants.

6.4. Error Analysis

The primary source of error in deriving fundamental parameters for the stars in the sample is the calculation of $E(B-V)$. This has three components: 1) the spread in possible T_{eff} values assigned once stars are spectrally classified (which we estimate to be ±500K), 2) the error introduced at the flux calibration stage of spectral extraction and also spectral extraction itself, and 3) the previously mentioned error from using the spectral fitting code to derive $E(B-V)$ by fitting with a blackbody spectrum. We numerically estimate the first two of these by running the spectral fitting code multiple times over the adopted range of input T_{eff} (±500K) for each of a sample of stars that were imaged multiple times on a night (and hence have 2 or 3 spectra). The resultant combined spread in retrieved $E(B-V)$ was adopted as the error produced by 1) and 2) specific to that star. For stars where only one spectrum had been taken we estimated the error from 2) and 1) from that derived for

[3]http://cxc.harvard.edu/sherpa/threads/index/html

[4]Model: xsmekal in sherpa

other stars observed on the same night for which multiple spectra were available (the error is more or less the same within a night). This error ranges from ∼10% in cases where repeat observations of spectra were most consistent with each other, up to ∼60% in the worst cases of extreme discrepancy between spectral extractions. This happened for moderate and also high S/N spectra, and varied both within a night as well as from night to night.

To calculate the error produced by the last of the factors, we ran the fitting code on a sample of 17 standard star spectra (types M5 V through A7 V) from the catalogue of Jacoby et al. (1984) to which we applied a range of fake values of interstellar reddening ($E(B-V)$ = 0.3–4.0) with the *fm_unred* command in IDL[5]. Each spectral standard was fit with the code in the same way as the program stars, using an input T_{eff} appropriate to its spectral type. The average in the difference between all retrieved and simulated $E(B-V)$ values over all spectral types at each step in simulated $E(B-V)$ was calculated and expressed as a percentage "error." Typically we find $\Delta E(B-V) \approx 50\%$ at $E(B-V) \approx 0.3$, ranging down to $\approx 6\%$ at $E(B-V) \approx 1.3$ (independent of spectral type). We linearly interpolate this trend to calculate the uncertainty produced by the fitting process at any $E(B-V)$. We combine this percentage error in quadrature with that calculated for the first two sources of error noted above, and convert to an error in column density N_H—this combined error is that quoted in table 4 in column 5.

The internal error from the χ^2 fitting process produces an estimate of the internal error in calculating N_H in this way—however, without including the errors arising from the extraction and flux calibration process this would be a large underestimate.

We note that we may still be underestimating the uncertainty in $E(B-V)$. We performed a further test of the fitting process by dereddening the program stars using *fm_unred*, and $E(B-V)$ as derived from our spectral fits and then visually comparing them to standard stars from Silva & Cornell (1992) and Jacoby et al. (1984) of similar spectral type. Although this generally shows a good fit between our spectra and the standard stars in the blue part of the spectra (∼4000–6700Å), redward of ∼7000Å many of our spectra (particularly those from the 2001 observing runs) drop off in flux below that expected in stars of the same type—if a similar drop-off at the blue end were present, we could be systematically overestimating $E(B-V)$ by ∼25%, since we only attribute any lack of flux at the blue end of the spectra to interstellar reddening. Since our fit to the spectrum is restricted to the range 5500–6700Å we believe this overestimation should be somewhat reduced.

The errors quoted in table 4 for $\log(F_x/F_R)$ and $\log(L_x)$ incorporate the error produced by uncertainty in N_H in calculating the X-ray flux and the error in the count rate (the

[5]http://idlastro.gsfc.nasa.gov/

photometric error in the R magnitude is small in comparison). However, in assigning a single model to all sources we may be overlooking the effect of the choice of spectral model on the flux. We investigate this effect by generating rate-to-flux conversion factors in the same way as before, but now substituting the MEKAL kT=1.0 keV model for a power law model with spectral index Γ=1.7 and also a MEKAL, kT=2.0keV model. In both cases, the S_C band flux is reduced by between 10% (at $N_H \approx 0.2\times10^{22}$ cm^{-2}) and 50% (at $N_H \approx 2.0\times10^{22}$ cm^{-2}). Both these spectral models have roughly the same rate-to-flux conversion at a given N_H. A model that has a larger soft band component to its emission (say, a MEKAL model with kT=0.5 keV) would cause the S_C rate-to-flux conversion factor to *increase* for any given N_H. Thus the errors quoted in $\log(F_x/F_R)$ and $\log(L_x)$ in table 4 should be considered as lower limits.

The other main source of error derives from our use of the model of Drimmel & Spergel (2001). In any given direction in the fields considered in this paper, it was found that significant changes in the run of A_V with distance were produced by varying the Galactic coordinates input into the code over the *Chandra* ACIS field of view. This is simply produced by variations of the theoretical model on these scales and is likely not representative of true structure in the absorbing interstellar medium, which may be large in this part of the Galaxy and is poorly modeled in the code. Within 20° from the GC, the Drimmel & Spergel (2001) model is at its most uncertain. The true distribution may lie somewhere between the 'rescaled' and non-rescaled A_V vs. distance derivation of the model. To quantify this source of error, we have measured how much the distance that we derive from the dust model varies over the *Chandra* field of view for a given value of A_V, generating a new plot of A_V against distance at each point. We use a simple five point grid to sample the variation within the *Chandra* FoV. The combination of the error in A_V from the spectral fitting technique and the uncertainty from the dust model was found to result in an error on the distance typically $\lesssim$60%. We adopt 60% as the error on the distances that we quote in table 4, and that we use to find the error in the X-ray luminosity and optical absolute magnitudes in these and subsequent tables.

7. Analysis

7.1. CVs discovered in the survey

From qualitative analysis of the spectra alone, we discovered two clear CV candidates in the GalCA field from the LDSS2 spectral sample—they are listed in Table 4e, sources XS00945B2_002 (Figure 6a) and XS00945H2_035 (Figure 6c)—hereafter CV-A and CV-C, respectively. Another source, XS53392B3_0001 (hereafter, CV-B), was imaged with LDSS2

in the SgrA$\star$ field, but the spectrum suffered from being on the edge of the slit and was not possible to extract. It was later re-observed by the IMACS instrument at Magellan—its IMACS spectrum is shown in Figure 6b. All three spectra show broad $H\alpha$ in emission. CV-A and CV-B also show emission lines of HeI.

CV-B was previously detected by ROSAT Position Sensitive, Proportional Counter observations of the GC regions (Sidoli et al. 2001), as their source '65,' but without further identification possible at the time. It was found to have a count rate of 1.9±0.3 cts ks^{-1} in the ROSAT band 0.1–2.4keV.

We present XSPEC[6] fits for the two X-ray bright CVs (CV-A and CV-B) in Figure 7 below. CV-C has too few counts to provide adequate signal to noise for spectral fitting. We use a bremsstrahlung emission plus photon absorption model for the fit to each spectrum. The results we derive are shown in table 6.

To further analyze these sources, we employ Quantile Color-Color diagram analysis, first presented in Hong et al. (2004); the technique allows us to derive X-ray spectral information despite low source counts. It involves placing sources on an X-ray color-color diagram by the median and quartile energy fractions of their source counts. As defined by Hong et al. (2004), any general quantile Q_x is calculated as:

$$Q_x = \frac{E_{x\%} - E_{lo}}{E_{up} - E_{lo}} \tag{3}$$

where $E_{x\%}$ is the energy below which the net counts is $x\%$ of the total number of counts between E_{lo} and E_{up}; we select E_{lo}=0.3 and E_{up}=8.0 keV (B_X band) for our analysis. We plot the ratio Q_{25}/Q_{75} against $\log_{10}[m/(1-m)]$ ($m(\equiv Q_{50})$ is the median). For a given spectral model, we overlay a grid of column density N_H and model parameter. The grid shape is dependent on the *Chandra* ACIS response function for the ObsID considered. Figure 7 shows QCCD plots and bremsstrahlung model grids for ObsID 53392, which includes CV-B (detected with ∼3500 counts in this ObsID) and unidentified sources from the SgrA$\star$ list with at least 107 counts, and ObsID 945, which includes all three CVs (CV-A and CV-B were detected in ObsID 945 with ∼300 counts, CV-C has only ∼26 counts).

For the CVs we use the plots to initially estimate a plausible spectral model. If we assume that a bremsstrahlung spectrum is representative of their X-ray emission, we can thus estimate their spectral properties. Our best estimates are given in table 6. For CV-A and CV-B, the quantile-derived parameters are in good agreement with the estimates from the XSPEC fits. For CV-C, we can only place weak constraints on N_H and kT, but the error

[6]http://xspec.gsfc.nasa.gov/docs/xanadu/xspec/index.html

bars are consistent with a typical CV spectrum of bremsstrahlung at ∼2–8keV. We suggest that these CVs are all of the DNe type.

7.2. Stellar X-ray Sources

7.2.1. Coronally Emitting Stars

Our sample of X-ray selected optical targets is likely to be dominated by coronally emitting stars, either on the main sequence, before (T Tauri stars[7]), or after (giants). Comprehensive studies of Solar neighborhood (distance $\lesssim$25 pc) stellar X-ray emission properties have been carried out using ROSAT X-ray All-Sky survey data (Voges 1992), for example Hünsch et al. (1998a) (giant and supergiants), Hünsch et al. (1998b) (main sequence and sub-giant stars) and Schmitt & Liefke (2004). ChaMPlane however, is the first survey with sensitivity to coronal stars far from the Solar Neighborhood, beyond ∼10pc (as a minimum) and more typically between ∼0.2–4.5 kpc. Since our S_C band of 0.5–2.0keV does not quite approximate the ROSAT band 0.1–2.4keV (a factor of ∼35% difference in flux at most, assuming a single temperature (1 keV) MEKAL spectral model), we generate fluxes and luminosities using the *sherpa* code in the ROSAT band. To compare firstly with the presumably normal, non-active star studies of Schmitt & Liefke (2004) and Hünsch et al. (1998b), we break down their stellar samples into the same brackets of T_{eff} or spectral type as our sample (for example, F2 to G2). Our derivation of the absolute magnitude of stars in our sample gives us some crude indication of luminosity subclass (Main Sequence V, Sub-Giant IV, and possible Giant III). We restrict our comparison to main sequence stars only. In Figure 8 below, we plot histograms of $\log(F_x/F_V)$ for each spectral type grouping for our stars,

[7]Optical ID 38933 in the SgrB2 field, and Optical ID 96733 in the G347b field: strong, narrow $H\alpha$ and CaII emission.

Table 6. CVs With LDSS2 Spectra

CV	SrcID	OptID	Hα−R (mag)	FWHM[a] Hα(Å)	EW[b] Hα(Å)	XSPEC N_H[d]	XSPEC kT(keV)	QCCD N_H[d]	QCCD kT(keV)
CV-A	945B2_002	196642	−0.66(3)[c]	26±3	−48±5	1.0±0.2	8.9±4.6	1.4±0.3	9±3
CV-B	53392B3_0001	134464	−0.63(4)	24±3	−81±7	0.5±0.03	7.3±0.9	0.7±0.4	8±1
CV-C	945H2_035	234913	−0.20(4)	31±3	−60±10	···	···	>1.4	···

[a]Full width at half maximum intensity of the Hα line

[b]Equivalent width of the Hα line.

[c]As of 2000. In 2003 Hα−R was measured at -0.194.

[d]N_H in units of 10^{22}cm^{-2}

removing objects without a reliable distance estimate or V magnitude, non-detections in the S_C band and T Tauri candidates also. We overlay the data from Schmitt & Liefke (2004) and Hünsch et al. (1998b), removing all binaries and active stars from these two samples, using information from the SIMBAD[8] online database to identify such cases.

With the exception of the M stars, for which there is some agreement at high values of $\log(F_x/F_V)$, we can clearly see a large discrepancy between our sample and those from the two references quoted. Combining the stars from F2 to M2 (from Figure 8, first 3 panels), a simple K-S test of the $\log(F_x/F_V)$ distribution for our sample and that of Schmitt & Liefke (2004) shows almost no agreement (less than 10^{-23} probability that they are the same). For stars of type M2 to M6, there is a 1.2% likelihood that they are the same. Next, we perform a K-S test comparison of the cumulative X-ray *luminosity* functions of our sample and that of Schmitt & Liefke (2004). We construct the X-ray luminosity function by spectral type grouping, defined as $\Phi(\log L_x)$—the space density of sources at L_x, per interval $\Delta \log L_x = 0.4$ (which makes 1 magnitude). We sum up the total number of sources within each luminosity bin, form the cumulative distribution and normalize to the total. However, since our survey is not complete in any sense, we attempt to correct for volume incompleteness using the $1/V_{max}$ method of Schmidt (1968). We define for each source a maximum distance at which it could have been detected by the *Chandra* telescope, by determining for each source's position on the detector and its *Chandra* ObsID a minimum count rate at which it could have been detected, and thus a flux (given the specification of D03 for N_H as a function of distance and assuming a MEKAL spectral model at 1.0keV). This distance defines a maximum volume: V_{max} within which the source could have been found given its luminosity. We then weight the contribution of each source to the cumulative distribution such that each source contributes $1/\mathrm{V}_{max}$ to the total in each luminosity bin, and then form the final normalized distribution; below in Figure 9 we show graphically the results of this test. We have divided our stellar sample into two halves: spectral types F2 to G8 and G8 to M6 to maximize the statistical sample. In each case we compare our sample with that of Schmitt & Liefke (2004), over the same range of spectral types. We have removed all giant star candidates from our sample (those stars with M_V more than 2 σ brighter than main sequence stars of that type) and all stars listed more than 2 sigma in $\log(F_x/F_V)$ above that expected for a main sequence star. The left hand panel in each case (a and c) shows the simple number counts based luminosity distribution; the right-hand panel (b and d) shows the $1/\mathrm{V}_{max}$ corrected version of the same.

In both subsets (F2 to G8, and G8 to M6 stars) the K-S test shows that the uncorrected distributions are different with >99% probability, although the early type stars—types F2 to

[8]http://simbad.u-strasbg.fr/

G8—show better agreement in the corrected K-S test: 15% probability that the distributions are the same versus 1.8% for G8 to M6. This demonstrates the luminosity bias of our flux-limited survey—we preferentially observe only the most luminous objects, and fail to detect the faint objects, and at the same time detect objects with X-ray luminosities above that expected for ordinary main sequence stars. In Figure 8, we also plot histograms of $\log(F_x/F_V)$ for active binaries from the survey of Dempsey et al. (1993) (RS CVn stars) and Dempsey et al. (1997) (BY Dra stars). A simple KS-test in $\log(F_x/F_V)$ between our sample of F2 to M2 stars and the BY Draconis-type sample shows reasonable, although not perfect, agreement: $\sim$15% probability that they are drawn from the same distribution (see Figure 10, upper left panel). Doing the same for the RS CVn stars indicates at best only $\sim$0.5% probability (Figure 10, lower left panel). The luminosity distributions however show poor agreement. The BY Dra and RS CVn stars match the LDSS2 sample with $\lesssim$0.1% probability (see Figure 10, right-hand panels)—exceeding the luminosities of the BY Dra systems, and falling short of the RS CVn X-ray luminosities. Applying the correction to $\log(L_x)$ (-0.3) and $\log(F_x/F_V)$ ($\sim +0.4$) as derived in § 6.2 (from our overestimation of N_H) would bring our sample into somewhat better agreement with the BY Dra systems.

In summary, what we can draw from this is that, on the evidence of $\log(F_x/F_V)$ distributions, our sample is likely to be largely dominated by coronally active binaries. There remains a significant probability that some additional component of non-active stars is present—perhaps differences in age (younger lower-main-sequence stars have higher X-ray luminosities) and metallicity are contributing to the difference. Notwithstanding this difference, we proceed under the assumption that some significant fraction of our high $\log(F_x/F_V)$ objects are active binaries. We present our best candidates in § 7.2.2.

7.2.2. Active Binaries

We attempt to single out our best candidates for active binary stars by their properties in both the optical and X-ray regions.

In the strict definition (see e.g. Dempsey et al. 1993), RS CVn stars are binary systems in which at least one star has strong CaII H and K emission, and which show periodic light variations due to star spots associated with magnetically active surface regions. The more active star is a subgiant or giant F, G or K star. They also show elevated levels of chromospheric and coronal activity (e.g. CaII H and K, and X-ray emission) when compared to normal stars of the same spectral type. BY Dra stars are typically binary F, G, K or M dwarf (i.e. main sequence) stars with strong CaII H and K emission and periodic light variations, and heightened X-ray emission with respect to normal stars of these types. From

a qualitative analysis of the $\log(F_x/F_V)$ distributions presented in Figure 8, it would appear that almost all of the stars in our sample are active in their X-ray emission at some level, compared to main-sequence stars. To be conservative in categorizing objects as 'active' however, we select our best candidates for stars of these types at a 2 σ level. We pick candidate RS CVn systems as objects with absolute visual magnitude M_V more than 2 standard deviations brighter than that expected for a main sequence star of the same type, and with $\log(F_x/F_R)$ (S_C band) greater than -5.0. This is to mimic the properties of RS CVn systems in the ROSAT sample of Hünsch et al. (1998a). Stars with M_V consistent with being on the main sequence, but with $\log(F_x/F_R)$ (S_C band) more than 2 σ greater than that expected for that spectral type (see Hünsch et al. 1998b) are designated as candidate BY Dra systems. All candidates identified in this way are listed in Table 7 below. As can be seen from Figure 10, our whole sample is similar to BY Dra systems in its overall X-ray/optical properties—correcting for the overestimation of N_H as noted in § 6.2 would reduce $\log(L_x)$ by $\sim$0.3 and bring two distributions into better agreement. Thus there may be many more BY Dra systems in our sample than noted in Table 7.

7.2.3. qLMXB candidates

A qLMXB system consisting of a black hole or neutron star and a main sequence star will most likely show strong $H\alpha$ in emission in its optical spectrum. Since the only objects showing $H\alpha$ in emission in this sample are either CVs (see § 7.1 above) or T Tauri stars (objects XS00944B0_025 and XS00737B3_016 in the SgrB2 and G347b fields respectively), we look to the example of GRO J1655 −40 (Zhang et al. 1994; Harmon et al. 1995; Bailyn et al. 1995) a known qLMXB, soft X-ray transient system, which consists of an F3–6IV *sub-giant star* secondary and an accreting black hole primary. This system shows $H\alpha$ in absorption in quiescence: the secondary star is luminous enough to hide the emission line produced by the accretion disk (see Figure 11b). Our spectral classification is not precise enough to ascertain the luminosity classes of stars in the sample, so to find analogs to this system we search for stars with spectral type earlier than K, with absolute magnitude M_V more than 2 σ higher than that expected for a main sequence star of that type (see table 5). We then look for stars with $\log(F_x/F_R)$ (S_C band) more than 2 σ greater than that seen in sub-giant stars in the survey of Hünsch et al. (1998a) (see Table 7, note b for the criteria we apply to find these objects). The error/spread on the values quoted in note b of Table 7 is $\sim$0.2. Note that this is based on a limited number of sources (about 7 per spectral type grouping, A, F or G). In Table 7 we list the one candidate we find after this search, together with the properties of GRO J1655 −40 as measured in this survey. Figure 11a presents the LDSS2 spectrum—although it has been flux calibrated, it still suffers from a marked drop off

in flux beyond 7000Å (see error analysis § 6.4). This is only a very tentative classification—it is equally possible that this object is an RS CVn system instead. However, we note that on the basis of its spectrum, and X-ray properties in quiescence alone, GRO J1655 −40 could be mistaken for an RS CVn system. Further variability analysis and detailed spectral followup is necessary to rule out this object as a black hole or neutron star binary system.

8. Constraints on the Galactic CV Density

A main aim of the ChaMPlane survey is to investigate what constraints we can place on the local CV space density. For this paper, we follow a method similar to that of Grindlay et al. (2005). We define a maximum distance at which a CV would have been identified given the optical and X-ray detection limits of our survey. Given some model for the distribution of CVs in the Galaxy, we can predict the number we expect to be detectable in the corresponding volume and compare this with the number of candidate CVs and X-ray-$H\alpha$ emitters *actually* detected in the sample. We then examine the implications for the assumed value of the local (Solar Neighborhood) CV density.

Considering X-ray properties alone first, d_{max} is the distance out to which we can survey the Galaxy given an estimate of the CV X-ray luminosity distribution, and the detection limit for a particular *Chandra* observation, convolved with the run of N_H with distance in that direction. In Table 11 we give d_{max} for an assumed maximum CV luminosity of $10^{32.5}$ ergs s^{-1} in the H_C band (2–8 keV), a "typical" CV spectral model of bremsstrahlung emission at kT = 8 keV, and the D01 calculation of A_V (hence N_H) versus distance at the aimpoint of each field. Since the detector sensitivity falls off markedly beyond about 5′ from the aimpoint, we estimate d_{max} using a detection limit for each observation averaged over a 5′ radius. As a simple approximation, we assume that CVs are distributed in the Galaxy with some exponential scale height h in the z direction: $\mathrm{n}_{CV} \propto \exp^{-d(\sin b)/h}$, with n_{CV} the CV space density and b the galactic latitude. This is probably a reasonable assumption for the regions surveyed in this paper (provided we are only considering the distribution within ∼3 kpc of the Solar neighborhood). Following Grindlay et al. (2005), we consequently utilize the formalism of Tinney et al. (1993) in constructing an effective detection volume V_{eff}, as defined by d_{max}:

$$V_{eff} = \Omega \left(h/\sin|b|\right)^3 \left[2 - \left(\chi^2 + 2\chi + 2\right) \exp\left(-\chi\right)\right] \tag{4}$$

where $\chi = \mathrm{d}_{max}(\sin \mathrm{b})/\mathrm{h}$ and Ω the solid angle subtended by the ACIS field of view. V_{eff} corrects the *geometric* volume in which we search for the non-uniformity of the CV space density. For the ACIS-S observation J1655 we use the full 8′× 8′ field of view to calculate

Table 7. qLMXB, BY Dra and RS CVn candidates from our sample

SrcID	OptID	Type	Counts[a]	N_H 10^{22}cm^{-2}	$\log(F_x/F_R)$ (S_C)	Dist. (kpc)	$\log(L_x)$ (S_C)	M_V mag	NM	P(Ran)
qLMXB[b] candidates										
099B6_014	113239	midG	85±10	0.44±0.10	−2.3±0.4	2.2	31.0±0.3	2.50±0.96	1	0.056
099B7_003[c]	302832	F3–6IV	64±9	0.58±0.10	−3.0±0.4	2.8	30.9±0.2	1.17±0.91	1	0.015
BY Dra candidates										
099B7_029	263293	F/G?	18±6	0.70±0.24	−1.9±0.6	4.0	30.6±0.4	4.70±1.82	1	0.064
737B2_015	267161	G?	56±9	0.55±0.18	−1.2±0.5	2.5	31.0±0.5	5.89±1.44	1	0.049
737B3_007	311764	midG	18±6	0.72±0.11	−1.2±0.4	3.0	30.9±0.6	6.45±0.95	1	0.206
945B3_007	179593	G?	12±5	0.49±0.19	−1.6±0.5	0.8	29.5±1.5	8.53±1.51	1	0.021
RS CVn candidates										
944B3_004	251487	lateG	209±16	0.64±0.21	−3.2±1.1	1.0	30.6±1.4	1.31±1.63	1	0.014
099B6_004	358172	early/midG	13±5	0.79±0.19	−2.9±0.5	3.9	31.0±0.3	1.03±1.49	1	0.032
099B7_016	325171	G/K	21±6	0.80±0.19	−2.8±0.5	4.0	31.0±0.2	1.15±1.49	1	0.046
099B7_028	275985	G?	11±5	0.88±0.19	−3.6±0.7	4.5	30.4±0.6	0.76±1.49	1	0.092
737B1_002	154326	G?	9⋆±5	1.32±0.15	−2.8±0.6	4.2	31.0±0.7	1.76±1.25	1	0.770
737B2_013	281818	lateG	17±5	0.68±0.19	−3.0±0.5	2.8	31.0±0.6	1.42±1.48	1	0.041
737B2_014	268928	lateK	13±5	0.70±0.21	−2.7±0.5	2.9	30.8±0.6	3.02±1.59	1	0.040
737B3_026	223728	earlyK	9±5	1.07±0.12	−2.3±0.5	3.7	30.9±0.6	3.74±1.09	1	0.062

[a]See Tables 4a–e for explanations of headers. The error on the distance is ≈60%.

[b]For inclusion in this table as a qLMXB candidate, star must have $\log(F_x/F_R)$, (S_C) more than 2 σ greater than −3.6 (A-type), −4.0 (F-type, F/G-type), −3.2 (G-type).

[c]This is GRO J1655 −40, a known black hole qLMXB.

Table 8. CV Detection Constraints for the Five Chandra ObsIDs

ObsID	Field	CR limit[a] (ksec^{-1})	$\mathrm{dmax}_{32.5}$[c] (kpc)	$\mathrm{CV}_{32.5}$[d]	X-detect[e] (%)	O-detect[f] (%)	$\mathrm{ID}_{32.5}$[g]	Found
99	J1655	0.258	29.3	21.2	12.3±0.2	0.70±0.05	0.15	0(1)[h]
737	G347b	0.305	15.75	37.3	4.1±0.2	0.67±0.05	0.25	0
944	SgrB2	0.126	14.4	65.0	3.4±0.2	0.07±0.01	0.04	0
945	GalCA	0.305	11.3	22.6	3.0±0.2	0.13±0.02	0.03	2
53392	SgrA⋆	0.061	39.5	1232.7	1.7±0.02	0.011±0.002	0.15	1(1)[h]
Total	···	···	···	1378.8	···	···	0.62	3(5)

Note. — [a]The average count rate limit for this observation within 5′ of the *Chandra* aimpoint. [b]The number of X-ray sources detected in the B_X band. [c]The maximum distance we can detect a CV at $\log(L_x)$=32.5. [d]The number of CVs in the effective volume defined by the Tinney formula for this sky position and d_{max}. [e]The expected percentage of these CVs detected in X-rays. [f]The expected percentage of these CVs also detected optically. [g]The resultant number of CVs we expect to identify in this field. [h]This field includes one spectroscopically unconfirmed CV, see Table 9.

Ω (though this overestimates the detection probability, given that it doesn't fully account for the off-axis response). The GalCA pointing overlaps the SgrA$\star$ field of view, so this field only adds three-quarters of the full ACIS-I solid angle to the area of sky surveyed. The number of CVs we might expect to be present in such a volume is then $N_{CV} = n_{CV} \times V_{eff}$. We adopt a scale height of h = 200pc, and following the conclusions of Grindlay et al. (2005) among others, we adopt a local space density $n_{CV} = 1 \times 10^{-5}$ pc^{-3}. The number predicted to be in each field by our simple CV distribution model is given in table 11 as '$CV_{32.5}$'.

To model the detection rate of CVs, we assume firstly that the detection volume V_{eff} corrects for any spatial variations in the CV density distribution and populate each volume uniformly with a randomly distributed sample of 4.9×10^5 CVs from 0 pc up to d_{max} as determined for each field. We assign each fake CV an X-ray luminosity (in the H_C band) and X-ray to optical flux ratio $\log(F_x/F_V)$: we use X-ray data as collected by Grindlay et al. (2005), originally presented in Hertz et al. (1990), and the ROSAT survey (see: Verbunt et al. 1997; Schwope et al. 2002), to construct distributions in L_x and $\log(F_x/F_V)$ from which we randomly sample. We assume that these two parameters are uncorrelated (a simple scatter plot shows this to be the case for the 49 CVs in the ROSAT sample). For a bremsstrahlung X-ray spectral model at 8keV, the luminosity in the ROSAT band 0.1–2.4keV and our H_C band is approximately the same. We then derive an apparent V magnitude and observed X-ray flux, since we have an estimate of the interstellar extinction A_V as a function of distance (Drimmel et al. 2003). We examine what percentage of these CVs might be detected both optically and in X-rays in the photometry limit of our optical Mosaic survey, and the flux limit of the *Chandra* ObsID. We set our photometric detection limit at which we could have detected a CV via its $H\alpha - R$ color at a V magnitude of 23. The X-ray detection and optical identification percentages are given in table 11 below. The predicted number of actual CVs detected (optically) is given as $ID_{32.5}$. Since the optical detection limit is reached at only $\sim$2 kpc, the optical percentage quoted below is essentially equal to the 'X-ray-and-optical' detection percentage.

The full list of matches between our X-ray and optical source lists having $H\alpha - R < -0.3$, V < 23 and an optical signal to noise ratio > 1.4 is given in Table 12 below[9]. We restrict $H\alpha - R$ based on the work of Szkody et al. (2004) who find that only 17% of their sample of CVs from the Sloan Survey have an $H\alpha$ equivalent width below 28Å in emission (i.e. have $H\alpha - R > -0.3$). We can use spectra to rule out 6 of these as dMe, normal or T Tauri stars, and confirm 2 (CV-A and CV-B from this paper) as CV candidates. Note however, that CV-C is classified as a CV not by having $H\alpha - R < -0.3$ but by its $H\alpha$ line emission line which

[9]CV-C is not included because it has $H\alpha - R > -0.3$.

seems too broad (FWHM∼30Å: velocity width ∼1300 km s^{-1}) to be either a dMe star or T Tauri star (velocity width typically ∼200 km s^{-1}, Bertout 1989). The objects: optID 117714 in field SgrA⋆ and 182093 in field J1655 had no optical spectra taken in any ChaMPlane observing run. The final tally of CV candidates is thus: 1 (possibly 2) in SgrA⋆, 2 in the GalCA field and possibly 1 in J1655. This latter objects lies outside the main ACIS-S chip (S3) and its neighboring S4 chip—the large error circle size in which it is found means that even when looking exclusively at objects with $H\alpha - R < -0.3$ in the field, the probability it is a random match is high (>20%). We consider this a low probability CV candidate.

It is apparent that there are a large excess of CV candidates above the number predicted by our simulation: between 3 and 5 detected, with 0.62 predicted (i.e. a 62% probability of detecting one CV). In SgrA⋆ and GalCA fields considered in isolation there are a factor ∼10–70 too many. There are several factors which could be contributing to this difference which we shall discuss further in § 9.2.

9. Discussion

9.1. Stellar Coronal Emission

We have discovered a large sample of stellar coronal emission sources in our survey fields. Given the discrepancy we find between our distributions of $\log(F_x/F_V)$ and of $\log(L_x)$ and those of ordinary main sequence stars, a significant fraction of these are almost certainly active binaries, of either RS CVn or BY Dra type. Without further follow-up observations it is difficult to assign individual types beyond our tentative candidate list in table 7. Our sample of stars earlier than M2 is clearly different from that of ordinary stars in both these properties—here, non-active stars probably constitute a lesser fraction of the total. This is because our survey is flux-limited, and hence biased towards detecting intrinsically bright X-ray sources (high $\log(L_x)$, i.e. the active stars) and since our spectral sample is prone to saturation effects below $R \sim 15$, we are only able to look at faint optical sources (biasing towards higher $\log(F_x/F_V)$). Yet, our sample does not exactly match that of either type of active stars in its X-ray luminosity distribution, or $\log(F_x/F_V)$. This is because of a number of factors. 1) The X-ray spectral model choice is a strong influence on our calculated X-ray fluxes. We have opted for simplicity for a single temperature, kT = 1.0 keV MEKAL spectral model and yet almost all stellar coronal sources are best fit by at least two temperature components. Ordinary stars typically have $\mathrm{kT}_{low} \approx 0.13$ keV and $\mathrm{kT}_{high} \approx 0.85$ keV, while active stars such as RS CVn systems have $\mathrm{kT}_{low} \approx 0.17$ keV and $\mathrm{kT}_{high} \approx 1.41$ keV. Thus a significant contribution to the flux may be missed. We experimented with our spectral model choice (two-temperature versus single temperature) to test the effects of this and

Table 9. $H\alpha - R < -0.3$ Objects

OptID	$H\alpha - R$	R	Spectrum	$\log(F_x/F_R)$
J1655				
182093	-0.428	21.8	None	$< -0.99^{\star}$
306209	-0.323	21.1	dMe	-0.9 ± 0.4
411192	-0.344	19.5	dMe	-1.5 ± 0.5
G347b				
128771	-0.327	17.0	T Tauri	-2.5 ± 0.4
GalCA				
196642	$-0.661^{\dagger}$	20.3	CV	1.2 ± 0.6
SgrB2				
38933	-0.608	16.8	T Tauri	-2.7 ± 0.5
277618	-0.618	19.8	G?	-2.5 ± 0.5
SgrA				
42300	-0.313	19.2	dMe	-2.5 ± 0.9
117714	-0.631	22.7	None	-1.5 ± 0.5
134464	-0.629	21.8	CV	-0.1 ± 0.9

Note. — †This value of $H\alpha - R$ was recorded in 2000. In 2003 it had dropped to -0.182. *Undetected in S_C band—estimated upper limit to flux ratio.

found that the error incurred for low N_H objects ($\log(N_H) < 22.4$) was typically $\lesssim$20%. Above this column density the error climbed to $\sim$50%, but since this is not the case for most sources in this sample, this source of error is likely not the biggest contributor to this discrepancy. 2) The large error in our distance derivation for each object, produced by our reliance on the dust model of D01 is also potentially very important, and may also help explain why our derived luminosity distributions are so discrepant. The ratio $\log(F_x/F_V)$ has no dependence on the D01 model—only on our spectral fitting technique which produces $E(B-V)$ and hence N_H. However, Figures 4 and 5 show that perhaps we are systematically overestimating A_V. Decreasing this parameter would increase $\log(F_x/F_V)$ by between 0.3 and 0.5—a result which would make our sample look yet more like active stars of BY Dra type. Large uncertainties in the distances we derive, arising from the D01 model make it difficult to assess any systematic errors in the L_x or M_V that we derive, which determine the RS CVn content of the sample. We await the release of the updated model of Drimmel which should help address this question for these Galactic bulge fields.

Can we say anything about a difference in the stellar population discovered by our survey versus the nearby studies of stars using ROSAT? Our stellar coronal source sample appears likely to be a mix of both coronally active (RS CVn and BY Dra) and ordinary stars. To specifically compare the stars of these types in our sample with those found by ROSAT would require significantly improved spectral, variability and orbital analysis to more precisely classify our objects and tease out the contributions of age, metallicity, and binarity that might also be contributing to the observed differences the luminosity and X-ray to optical flux ratio.

9.2. Space Density of Cataclysmic Variables

Our simplistic approach to modelling the CV detection rate in our survey fields also yields possibly significant discrepancy with our observations for two out of the five fields. What factors are contributing to the incorrect estimation of the CV detection rate? 1) The dust model of D01. We assume that a single relationship between A_V and distance is applicable over the whole $16' \times 16'$ *Chandra* field of view yet extremes in the level of extinction are observed directly in infrared images of the SgrA$\star$ and GalCA fields (see e.g. Laycock et al. 2005). The model overlooks this small scale variability across each field. Thus if there were some covering factor of higher column density gas and dust across each field or regions of significantly lower extinction, we would expect to alter the number of predicted CVs detected. A factor of 1.5 decrease in the amount of extinction as a function of distance is necessary to produce the factor $\sim$2 increase in the overall prediction for CV detections

in these fields, whereas a factor of at least ∼10 in number of CV detections is required to solve the discrepancy for SgrA⋆. 2) We have assumed no radial component in our model CV space distribution yet it is likely that there is some increase in the space density of CVs as we approach the Galactic Center. Thus we are underestimating the true number of CVs present in each volume, before we apply our detection criteria. This may only be a minor correction, since our optical detection and spectroscopic identification limit restricts us to looking in the nearest ∼3 kpc to the Sun. Some additional work on improving how we model where the CVs are in our volume, and how many we expect to be in this volume is important to establish by how much we are underestimating N_{CV}. Such a modification would appear to be most necessary for the two fields closest to the Galactic Center: SgrA⋆ and GalCA. 3) Are we approximating the scale height h, and the local value of the CV density, n_{CV} incorrectly? It is difficult to establish this definitively. Patterson (private communication) recommends a smaller scale height h=150 pc on the basis of local CV surveys. Implementing this affects only fields J1655 and G347b (for the other fields the effect is negligible). This would reduce the *predicted* number of CVs by a factor of 2, and 1.3 respectively for these fields—further in line with our lack of CVs detected in these fields. Our sample is too small to be used to argue for a change in the local CV space density, given our large uncertainties in calculating detection rates given the dust model and our simple Galactic CV distribution model, although our results at face value require an increase in this parameter. 4) Are we mistaken in restricting our detection solid angle to the inner 5′ of the *Chandra* field of view and assuming zero sensitivity outside this? Including the outer parts of the detector (or for ACIS-S including the other S-chips) increases the detection area by a factor ∼3. Although the count rate limit beyond 5′ is considerably lower than at the aimpoint, it would increase the predicted detection rate slightly. However, the increase in predicted CV numbers would be small in comparison with other effects discussed above. Only CV-C is further than 5′ from the aimpoint in this case.

In summary, it would appear that factor 2) the dust extinction model is the most significant contributor to the discrepancy between our simulated numbers of CV detections and the actual detected sample in this paper. However, incorporating a better 3-dimensional model of the Galactic CV distribution would help to understand if 3) the local CV space density we have assumed is incorrect. Results from the much larger distribution of Galactic Bulge fields now included in ChaMPlane will be decisive in determining the CV space density and Galactic distribution.

10. Conclusion

We have carried out optical and X-ray spectral analysis on a sample of X-ray detected optical sources in the Galactic plane, using a combination of optical spectral fitting and quantile X-ray analysis to obtain the extinction $E(B-V)$ and hence A_V and hydrogen column density, N_H towards each object. We combine these estimates with the work of Drimmel & Spergel (2001) who present a three-dimensional dust model of the Galaxy in order to derive A_V as a function of distance in any direction, and thus further derive a distance to each object.

We present the discovery of a population of stellar coronal emission sources, detected by *Chandra* in five fields towards the Galactic bulge. The majority of these are likely to be active star systems, of RS CVn or BY Dra type. We find no strong evidence that we have sampled from stars with significantly different properties from local, similarly active stars. We report the properties of the most probable RS CVn and BY Dra-type candidates from our sample, and identify one possible qLMXB candidate also. We note that this latter object could instead be an RS CVn system. High resolution optical spectra can make this clear.

We report the discovery of three X-ray detected CVs in the direction of the Galactic Center. All three are consistent with having an X-ray spectrum consisting of bremsstrahlung at kT $\approx$ 8keV, and are within $\approx$2 kpc of the Sun. An additional 2 CVs are indicated by our photometry and X-ray data, and can be tested with spectra using IMACS at Magellan.

The numbers of CVs detected in our survey is consistent with a local CV space density of $\sim 10^{-5}$ pc^{-3}, and a scale height $\sim$200pc. However, there is considerable uncertainty in the model we use to predict extinction as a function of distance and hence derive the number detected in our survey. Further work on this aspect, and on better modelling the CV content of our fields is desirable to improve our constraints.

The author would like to thank John Silverman for collecting the LDSS2 spectral data during the 2001 run. This research has made use of the SIMBAD database, operated at CDS, Strasbourg, France and the NASA Astrophysics Data System. This work is supported in part by NASA/*Chandra* grants AR1-2001X, AR2-3002A, AR3-4002A, AR4-5003A, AR6-7010X, NSF grant AST-0098683, and the *Chandra* X-ray Center. We thank NOAO for its support via the Long Term Survey program.

REFERENCES

Andrillat, Y., Jaschek, C., & Jaschek, M. 1995, A&AS, 112, 475

Bailyn, C. D., Orosz, J. A., McClintock, J. E., & Remillard, R. A. 1995, Nature, 378, 157

Bertout, C. 1989, ARA&A, 27, 351

Bessell, M. S. 1991, AJ, 101, 662

Brand, J. & Blitz, L. 1993, A&A, 275, 67

Carquillat, M. J., Jaschek, C., Jaschek, M., & Ginestet, N. 1997, A&AS, 123, 5

Cox, A. N. 2000, Allen's astrophysical quantities (Allen's astrophysical quantities, 4th ed. Publisher: New York: AIP Press; Springer, 2000. Edited by Arthur N. Cox. ISBN: 0387987460)

Dame, T. M., Hartmann, D., & Thaddeus, P. 2001, ApJ, 547, 792

Dempsey, R. C., Linsky, J. L., Fleming, T. A., & Schmitt, J. H. M. M. 1993, ApJS, 86, 599

—. 1997, ApJ, 478, 358

Dopita, M. A. & Sutherland, R. S. 2003, Astrophysics of the diffuse universe (Astrophysics of the diffuse universe, Berlin, New York: Springer, 2003. Astronomy and astrophysics library, ISBN 3540433627)

Drimmel, R., Cabrera-Lavers, A., & López-Corredoira, M. 2003, A&A, 409, 205

Drimmel, R. & Spergel, D. N. 2001, ApJ, 556, 181

Gray, D. F. 1992, The observation and analysis of stellar photospheres (Cambridge Astrophysics Series, Cambridge: Cambridge University Press, 1992, 2nd ed., ISBN 0521403200.)

Grindlay, J., et al. 2003, Astronomische Nachrichten, 324, 57

Grindlay, J. E., et al. 2005, ApJ, 635, 920

Harmon, B. A., et al. 1995, Nature, 374, 703

Hertz, P., Bailyn, C. D., Grindlay, J. E., Garcia, M. R., Cohn, H., & Lugger, P. M. 1990, ApJ, 364, 251

Hong, J., Schlegel, E. M., & Grindlay, J. E. 2004, ApJ, 614, 508

Hong, J., van den Berg, M., Schlegel, E. M., Grindlay, J. E., Koenig, X., Laycock, S., & Zhao, P. 2005, ApJ, 635, 907

Houk, N., Swift, C. M., Murray, C. A., Penston, M. J., & Binney, J. J. 1997, in ESA SP-402: Hipparcos - Venice '97, 279–282

Howarth, I. D. 1983, MNRAS, 203, 301

Hünsch, M., Schmitt, J. H. M. M., & Voges, W. 1998a, A&AS, 127, 251

—. 1998b, A&AS, 132, 155

Jacoby, G. H., Hunter, D. A., & Christian, C. A. 1984, ApJS, 56, 257

Johnson, H. L. 1966, ARA&A, 4, 193

Laycock, S., Grindlay, J., van den Berg, M., Zhao, P., Hong, J., Koenig, X., Schlegel, E. M., & Persson, S. E. 2005, ApJ, 634, L53

Mewe, R., Gronenschild, E. H. B. M., & van den Oord, G. H. J. 1985, A&AS, 62, 197

Mikami, T. & Heck, A. 1982, PASJ, 34, 529

Muno, M. P., et al. 2003, ApJ, 589, 225

Patterson, J. 1998, PASP, 110, 1132

Predehl, P. & Schmitt, J. H. M. M. 1995, A&A, 293, 889

Schlegel, D. J., Finkbeiner, D. P., & Davis, M. 1998, ApJ, 500, 525

Schmidt, M. 1968, ApJ, 151, 393

Schmitt, J. H. M. M. & Liefke, C. 2004, A&A, 417, 651

Schwope, A. D., Brunner, H., Buckley, D., Greiner, J., Heyden, K. v. d., Neizvestny, S., Potter, S., & Schwarz, R. 2002, A&A, 396, 895

Sidoli, L., Belloni, T., & Mereghetti, S. 2001, A&A, 368, 835

Silva, D. R. & Cornell, M. E. 1992, ApJS, 81, 865

Szkody, P., et al. 2004, AJ, 128, 1882

Taylor, A. R., et al. 2003, AJ, 125, 3145

Tinney, C. G., Reid, I. N., & Mould, J. R. 1993, ApJ, 414, 254

Torres-Dodgen, A. V. & Weaver, W. B. 1993, PASP, 105, 693

Verbunt, F., Bunk, W. H., Ritter, H., & Pfeffermann, E. 1997, A&A, 327, 602

Voges, W. 1992, The ROSAT all-sky X ray survey, Tech. rep.

Warner, B. 1995, Cataclysmic variable stars (Cambridge Astrophysics Series, Cambridge, New York: Cambridge University Press, —c1995)

Zhang, S. N., Wilson, C. A., Harmon, B. A., Fishman, G. J., Wilson, R. B., Paciesas, W. S., Scott, M., & Rubin, B. C. 1994, IAU Circ., 6046, 1

Zhao, P., Grindlay, J. E., Hong, J. S., Laycock, S., Koenig, X. P., Schlegel, E. M., & van den Berg, M. 2005, ApJS, 161, 429

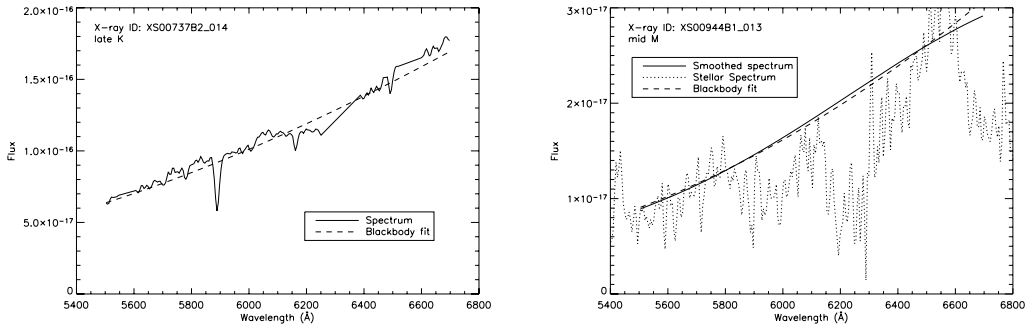

Fig. 1.— Two example fits to spectra from the LDSS2 sample. The panel for the M star (right) also shows the polynomial fit to the spectrum, to which the blackbody curve was subsequently fit. The flux scale in each case has units: ergs $s^{-1}cm^{-2}$ $Å^{-1}$.

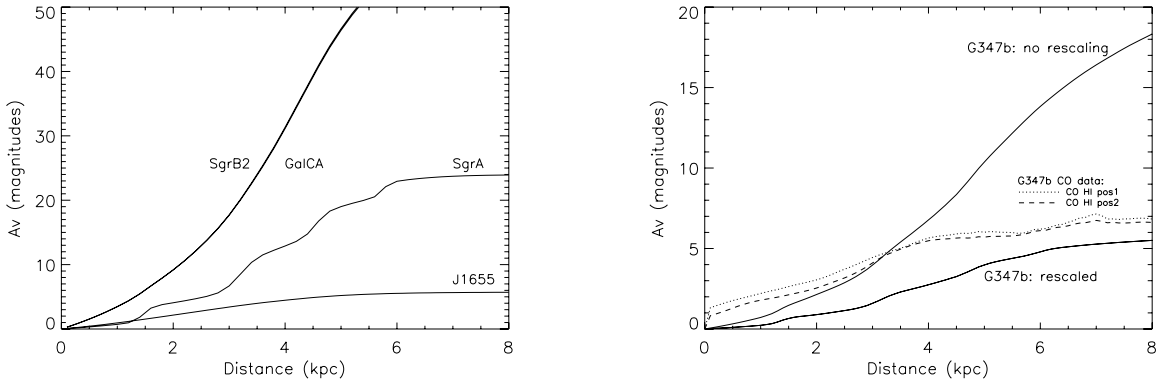

Fig. 2.— Plots of A_V (re-scaled values) versus distance from the model of Drimmel & Spergel (2001) for the five *Chandra* fields. For field G347b (right-hand plot) we show the results of both rescaled and non-rescaled A_V versus distance from this paper, and also overplot our own results, as derived from CO+HI observations. See § 6.2 for a description.

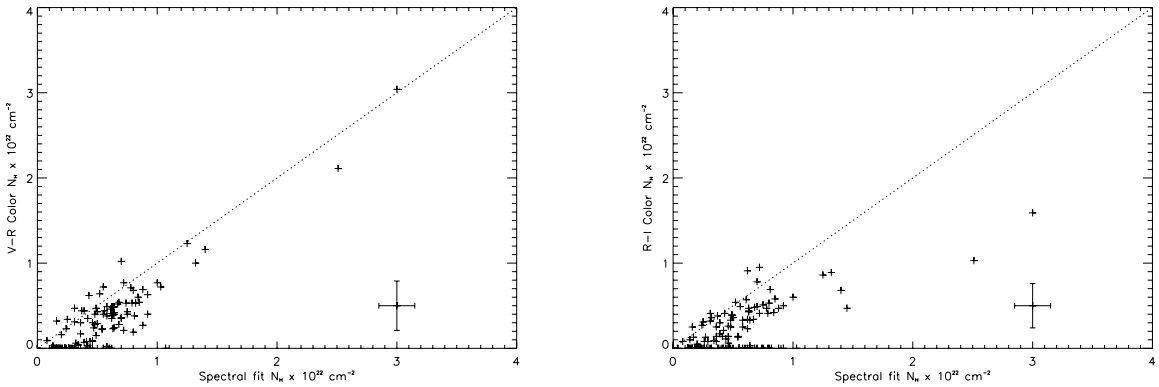

Fig. 3.— Plots of hydrogen column density for all stars in the sample, as derived from the different methods detailed in § 6.2. Typical error bars are plotted and an overlay of N_H(Color)=N_H(Fit) is shown for reference. $N_H = 0$ values from either the $V - R$ or $R - I$ colors are a result of the lack of sensitivity of this method to small N_H (below about $5{\times}10^{21}$ cm^{-2}) or a non-detection in one of the photometric bands.

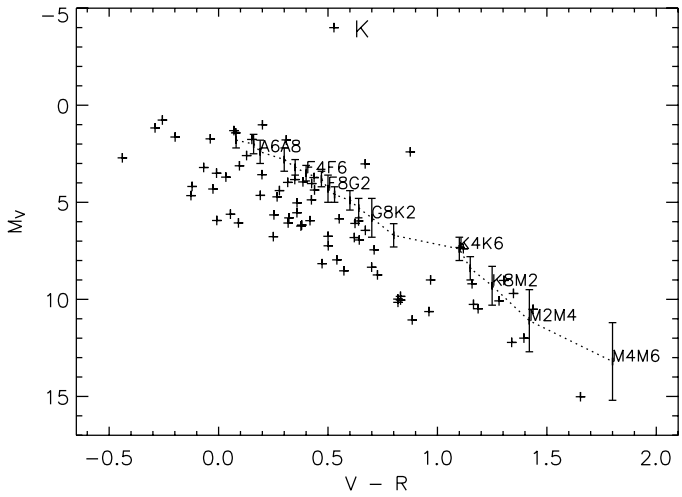

Fig. 4.— A Color-Magnitude diagram of the stars in the LDSS2 sample. We plot $M_V = V - 5\log(\mathrm{dist}) + 5 - A_V$, and $(V-R)_0 = V - R - 0.781E(B-V)$. The star marked 'K' is the K giant in SgrB2, Optical ID 234977. The dotted curve and spectral type labels are from Cox (2000) and the error bars show the range of M_V for spectral type range plotted.

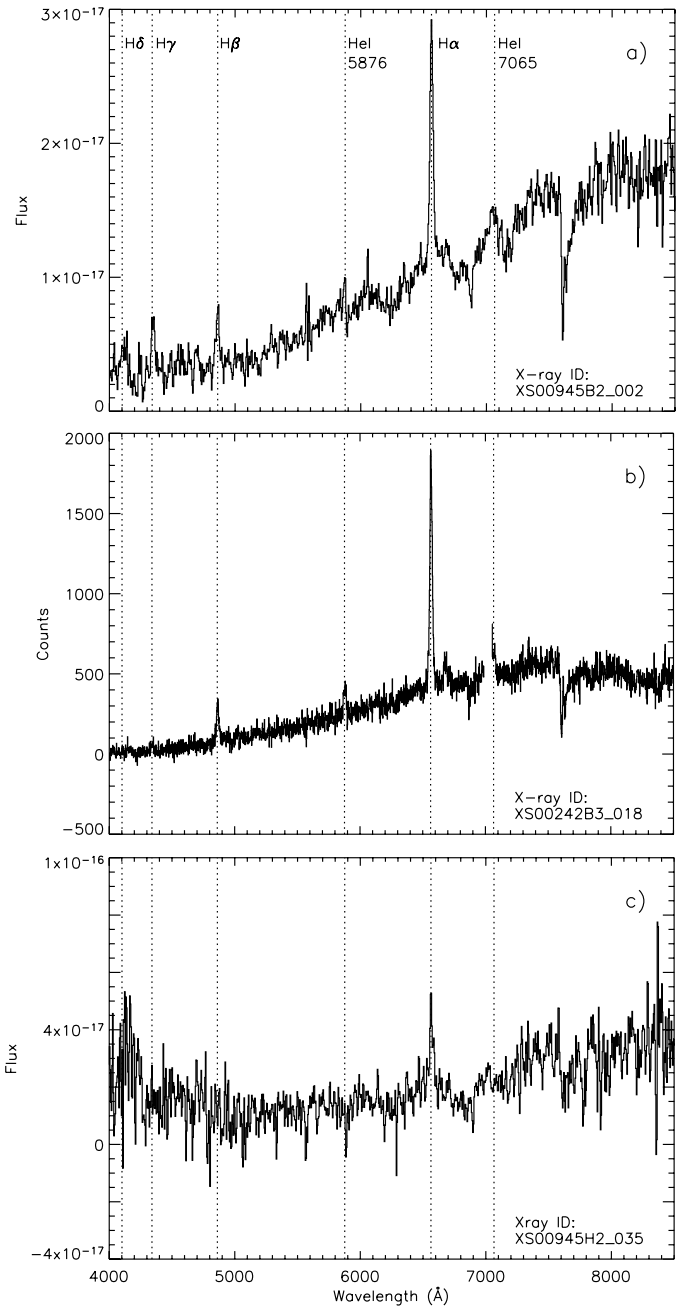

Fig. 5.— The three CVs discovered in the five *Chandra* fields in this paper. The LDSS2 spectra for CV-A and CV-C have y-axis units ergs s^{-1} cm^{-2} Å. The IMACS spectrum for CV-B was not flux calibrated and has y-axis units in raw counts. The region 6990–7500Å has been removed from CV-B as it covers a CCD chip gap.

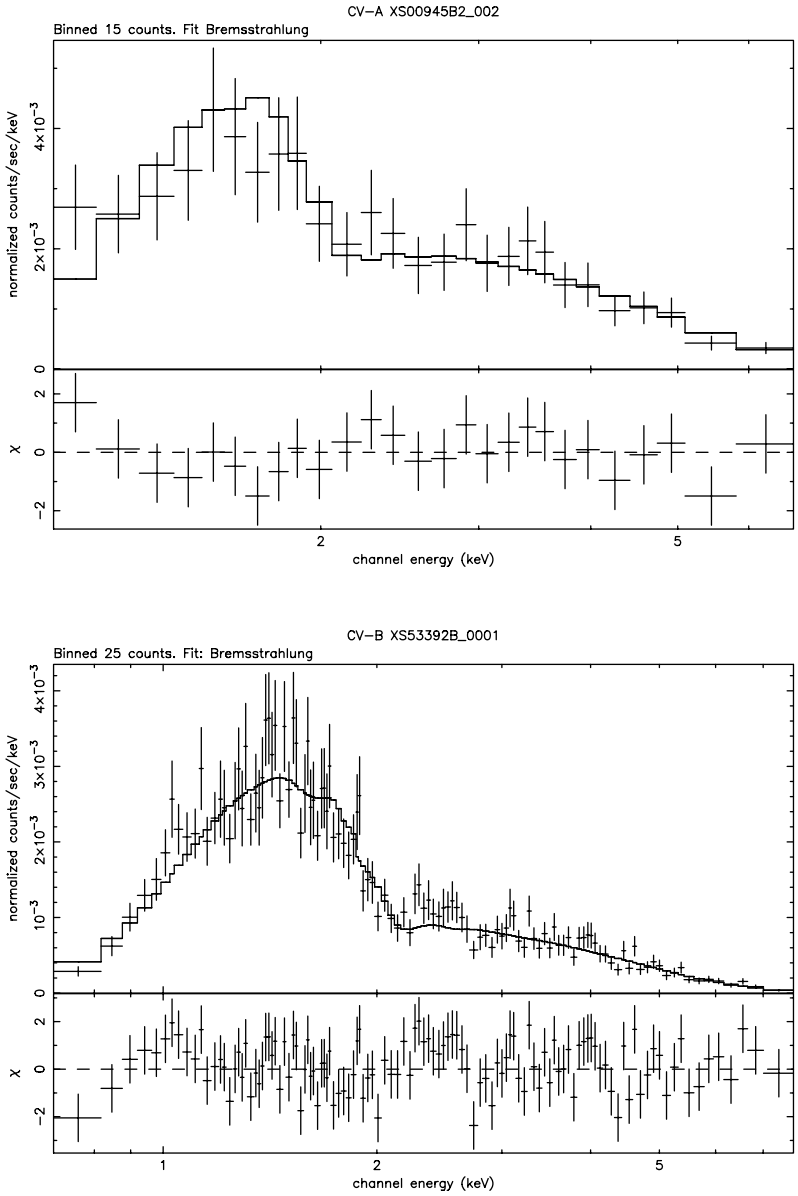

Fig. 6.— XSPEC fits to the X-ray data for the CV-A and CV-B detected in this survey. Upper spectrum, CV-A: 438.0 net counts (B_X band), lower spectrum, CV-B: 3536.1 net counts. We plot the spectrum plus fit, and in the lower panel in each case the residuals of the spectrum divided by the fit.

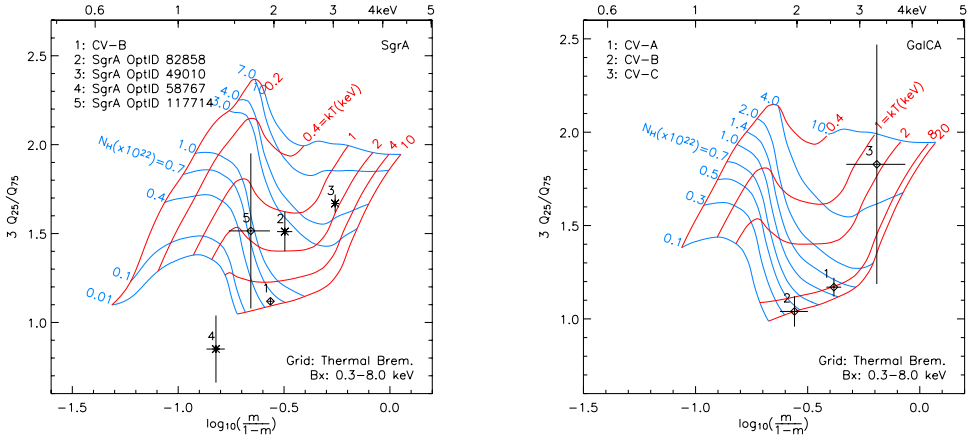

Fig. 7.— QCCD plots for ObsIDs 53392 (SgrA⋆) and 945 (GalCA) showing the positions of the non-identified sources from the SgrA⋆ field with at least 107 counts (left) and the three CVs (right).

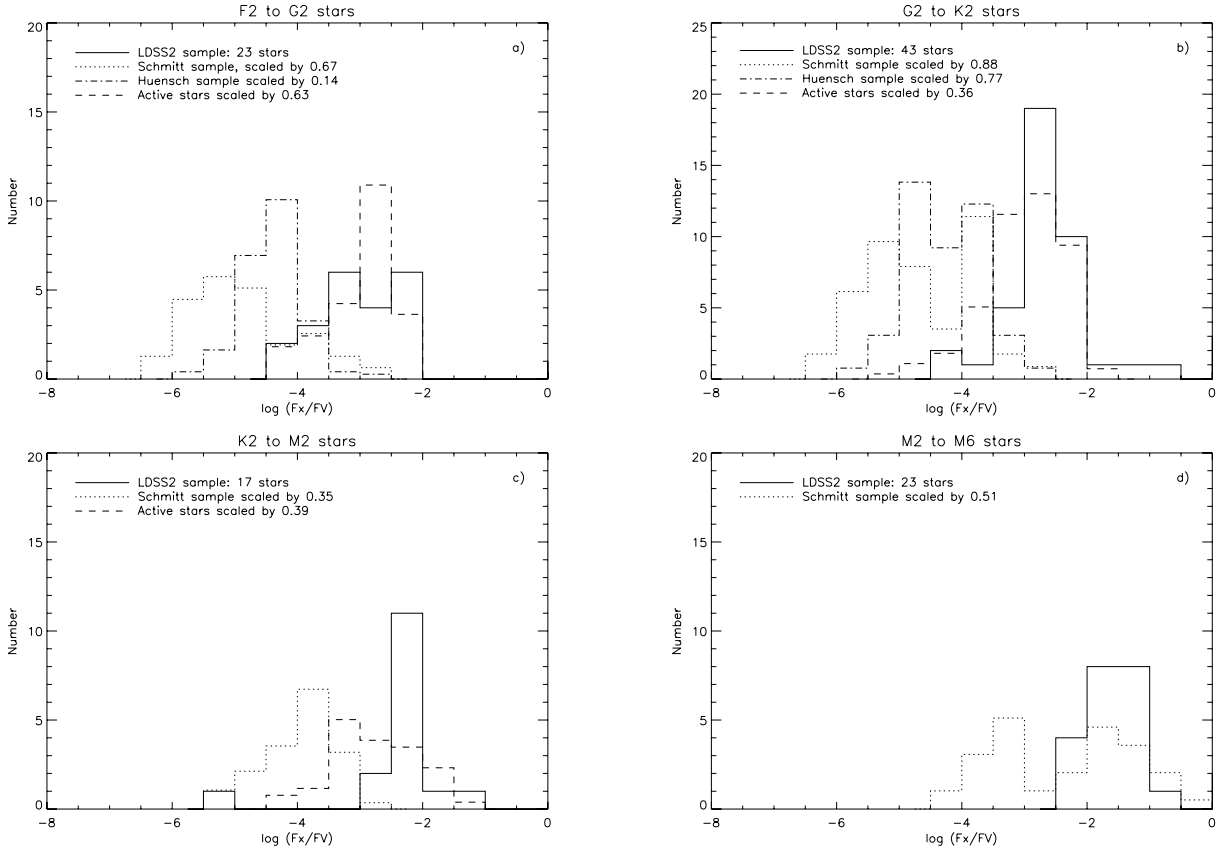

Fig. 8.— Histograms by spectral type grouping of the X-ray to optical flux ratio of our stellar sample, overplotted with data from the studies of Schmitt & Liefke (2004) (dotted) and Hünsch et al. (1998b) (dot-dashed). The dashed line shows active stars (both RS CVn and BY Dra types) from Dempsey et al. (1993) and Dempsey et al. (1997). We classify 62–77% of our M stars as dMe from their Hα emission.

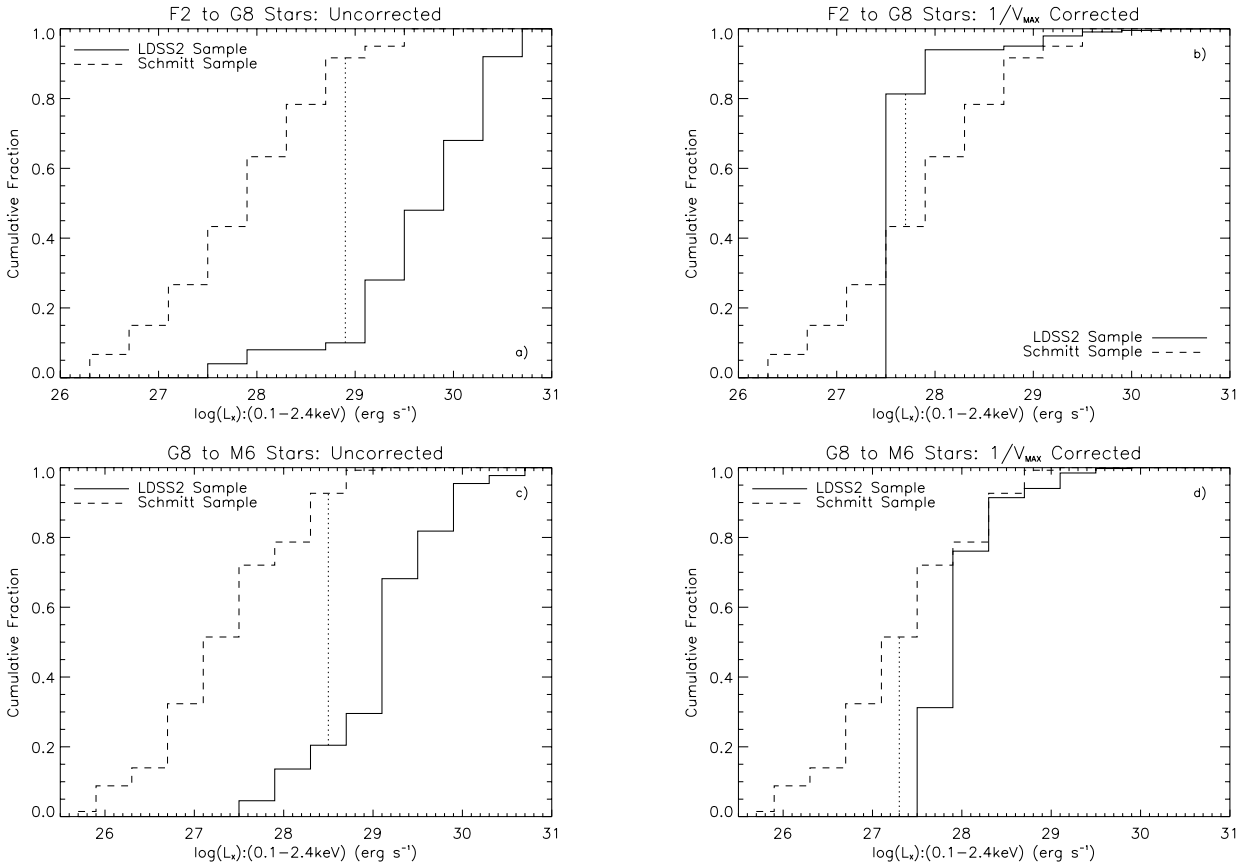

Fig. 9.— K-S test plots for our stellar coronal sample. We divide our sample into stars from type F2–G8 (50 stars) and G8–M6 (40 stars). In each case, the left hand panel shows the uncorrected, number based density distribution. The right-hand panel shows the $1/V_{max}$ corrected version.

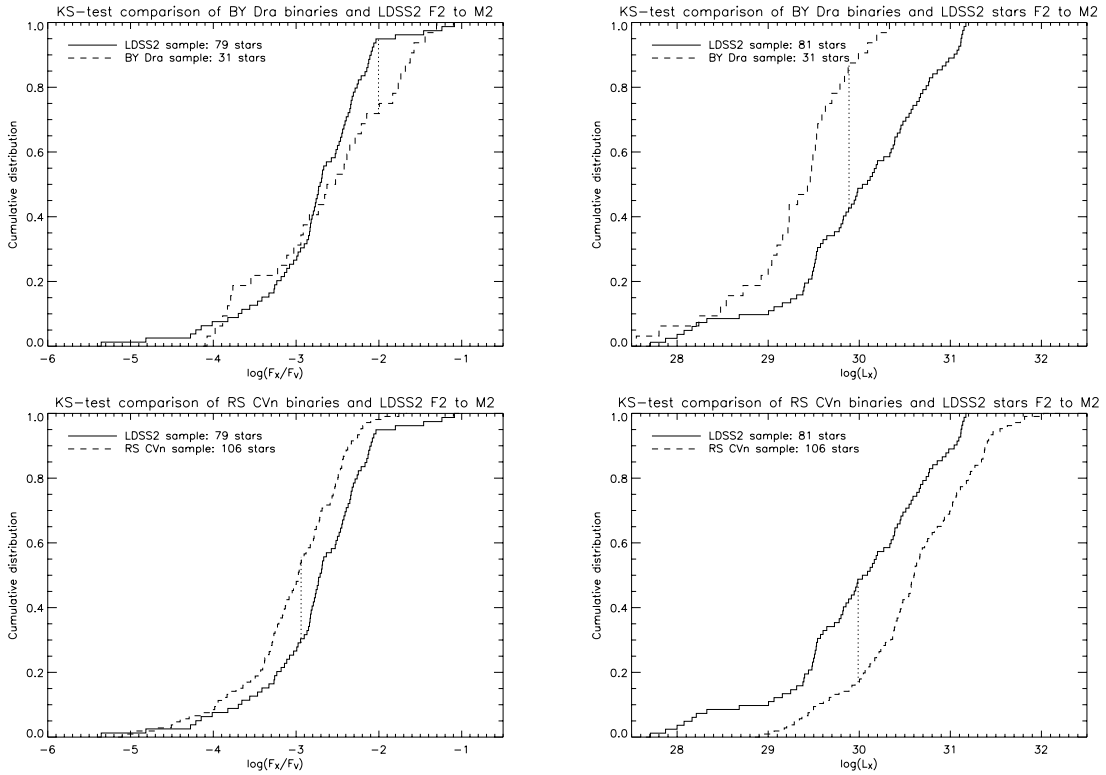

Fig. 10.— K-S test comparisons for our stellar coronal sample against BY Dra stars (upper panels) and RS CVn stars (lower panels). The left side plots compare $\log(F_x/F_V)$ and those on the right, $\log(L_x)$. We compare stars in both samples from spectral type F2 to M2 only. RS CVn and BY Dra data come from Dempsey et al. (1993) and Dempsey et al. (1997).

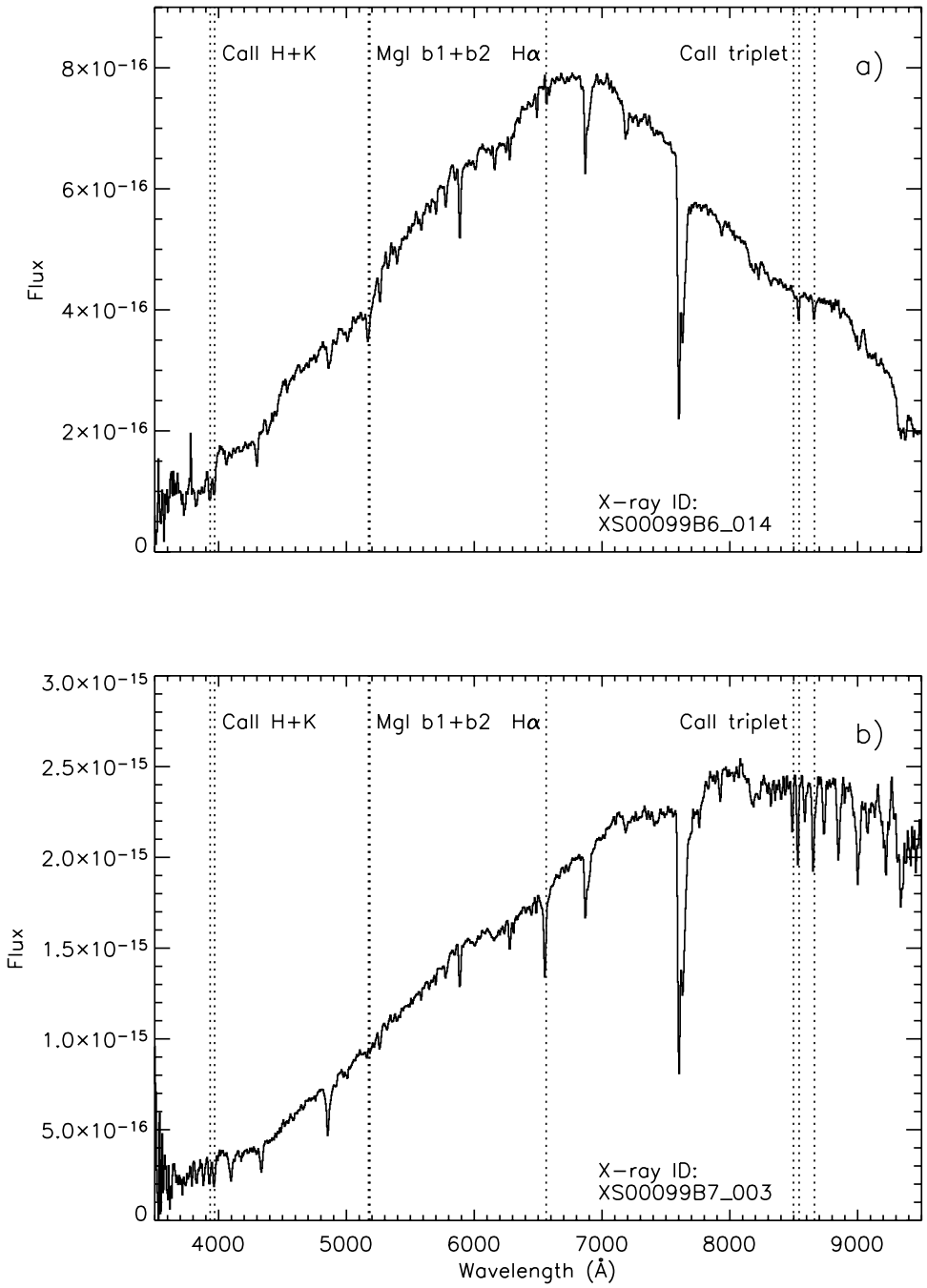

Fig. 11.— Upper spectrum: the qLMXB candidate found in our LDSS2 sample. Lower spectrum: GRO J1655 −40 as observed by LDSS2 from our June 2002 observing run. The flux scale has units: ergs s^{-1} cm^{-2} $Å^{-1}$. Important spectral lines are marked on the spectra for reference. The strongest spectral feature at λ7600 is telluric absorption by the Earth's atmosphere.